FIBER-OPTIC MAGNETOMETRY AND THERMOMETRY USING OPTICALLY DETECTED MAGNETIC RESONANCE WITH NITROGEN—VACANCY CENTERS IN DIAMOND

A Dissertation

by

SEAN MICHAEL BLAKLEY

Submitted to the Office of Graduate and Professional Studies of
Texas A&M University
in partial fulfillment of the requirements for the degree of

DOCTOR OF PHILOSOPHY

Chair of Committee,	Aleksei M. Zheltikov
Committee Members,	George W. Kattawar
	Alexei V. Sokolov
	Vladislav V. Yakovlev
Head of Department,	Peter M. McIntyre

May 2017

Major Subject: Physics

ABSTRACT

Nitrogen—vacancy diamond (NVD) quantum sensors are an emerging technology that has shown great promise in areas like high-resolution thermometry and magnetometry. Optical fibers provide attractive new application paradigms for NVD technology. A detailed description of the fabrication processes associated with the development of novel fiber-optic NVD probes are presented in this work. The demonstrated probes are tested on paradigmatic model systems designed to ascertain their suitability for use in challenging biological environments.

Methods employing optically detected magnetic resonance (ODMR) are used to accurately measure and map temperature distributions of small objects and to demonstrate emergent temperature-dependent phenomena in genetically modified living organisms. These methods are also used to create detailed high resolution spatial maps of both magnetic scalar and magnetic vector field distributions of spatially localized weak field features in the presence of a noisy, high-field background.

DEDICATION

This document is dedicated to the memory of William R. Trueblood.

"Oh! I have slipped the surly bonds of earth,

And danced the skies on laughter-silvered wings;

Sunward I've climbed, and joined the tumbling mirth

Of sun-split clouds, --and done a hundred things

You have not dreamed of --Wheeled and soared and swung

High in the sunlit silence. Hov'ring there

I've chased the shouting wind along, and flung

My eager craft through footless halls of air...

Up, up the long, delirious, burning blue

I've topped the wind-swept heights with easy grace

Where never lark or even eagle flew --

And, while with silent lifting mind I've trod

The high untrespassed sanctity of space,

Put out my hand, and touched the face of God."

- John Gillespie Magee, Jr.

ACKNOWLEDGEMENTS

I would first like to acknowledge my beloved wife Dr. Amber Trueblood and my esteemed advisor Dr. Aleksei Zheltikov.

Without the enduring love and support of my wife Amber, this document would not exist, and my graduate career would never have begun in the first place. Her steadfast patience and dedication to my future has been a source of immeasurable comfort and solace throughout the course of my studies.

Dr. Zheltikov gave me the opportunity to prove myself when no one else would. He has provided wise counsel, a steady guiding hand, and abiding patience during the ennui and occasional tumult of the last six years of graduate life. With his support I was allowed freedom to pursue interests of my choosing both in research and in my personal life, a fact that I am profoundly grateful for. Thanks to his efforts, my entire graduate career has been supported by his own startup funds and support from the Welch Foundation (grant number A-1801). He and Dr. Marlan Scully have supported my travel and conference attendances. For these things I am truly grateful.

I would also like to acknowledge the contributions of Dr. Ilya Fedotov and Dr. Phillip Hemmer to this research.

Ilya took me under his wing during his visits to Texas A&M and molded me into the experimentalist that I am today. He has been an absolutely vital element of our team, and a close personal friend. We have accomplished much together, and without his guidance our lab would remain an empty room.

Dr. Hemmer has been an invaluable resource for the development of our experimental plan, and has personally aided me in the advancement of our joint research endeavors. He opened his doors to our group when we had nothing but an idea, and his early support and guidance have sewn the seed for a crop that we will harvest for years to come.

I would also like to acknowledge my committee members Dr. George Kattawar, Dr. Alexei Sokolov, and Dr. Vladislav Yakovlev. Dr. Kattawar was instrumental in my decision to attend this university. Without his help, I would not be here today. Dr. Sokolov has been a crucial member of our team, and has provided vital material support and advice on our work. He has always had an open door for me. I would also like to thank Dr.Yakovlev for his support for our research in its early stages. He helped me get my feet wet in his lab in the early days of my research at this university, and for that I am profoundly grateful

I would like to thank my current and former group members Peter Zhokov, Evgeniy Serebryannikov, Nikolai Safronov, Hector Perez, Joe Becker, and Yusef Maleki, for their aid, advice, and hard work towards fulfilling all of our ultimate research goals.

I would also like to thank our esteemed collaborators Dr. Alexey Akimov, Masfer Al-Kahtani, Fahad Alghannam, and Abdurrahman Almethen, for their aid and devotion to our research, and my personal friends Steven Rodriguez, Nathan Rodriguez, Dawson Nodurft, Kelly Mader, Sasha Zhdanova, and Evan Stewart for being excellent friends and their help in providing me advice and a necessary distraction from the daily

grind of graduate school.

Finally I would like to acknowledge the support of my family for their undying love and support, my grandfather Dr. George Robert Blakley Jr. for his foundational contributions to my development as a scientist and as a person, and my mother and father Drs. Bob and Karen Blakley for helping me become the man I am today, and for always providing me with support and love, regardless of circumstance.

CONTRIBUTORS AND FUNDING SOURCES

This work was supervised by a dissertation committee consisting of Professor Aleksei Zheltikov [advisor] of the Department of Physics and Astronomy at Texas A&M University, Professors George Kattawar and Alexei Sokolov of the Department of Physics and Astronomy at Texas A&M University, and Professor Vladislav Yakovlev of the Department of Biomedical Engineering at Texas A&M University.

The data and analyses in the literature review depicted in section 2.4 were provided by Professor Aleksei Zheltikov of the Department of Physics and Astronomy at Texas A&M University and were published in 2015.

All other work for the dissertation was completed by the student under the advisement of Professor Aleksei Zheltikov and in collaboration with Professor Phillip Hemmer of the Department of Electrical and Computer Engineering at Texas A&M University, Professor Marlan Scully of the Department of Physics and Astronomy at Texas A&M University, Professors Ilya Fedotov, Evgeniy Serebryannikov, Aleksandr Lanin, and Andrei Fedotov of the Department of Physics at Moscow State University, Professor Lyubov Amitonova of the Institute for Nanotechnology at the University of Twente, Professors Alexey Akimov, Sergei Killin, and Vladimir Velichansky of the Russian Quantum Center, Hector Perez, Masfer Al-Kahtani, Fahad Alghannam, Abdurrahman Almethen, Yusef Maleki, and Joe Becker of the Department of Physics at Texas A&M University, Nikolai Safronov of the Department of Physics at Moscow State University, and Yulia Ermakova of the Institute of Bioorganic Chemistry at the Russian Academy of Sciences.

This work was made possible in part by the Welch Foundation under Grant Number A-1801 and by startup funds generously provided by Professor Aleksei Zheltikov of the Department of Physics at Texas A&M University.

Its contents are solely the responsibility of the authors and do not necessarily represent the official views of the Welch Foundation.

TABLE OF CONTENTS

Page

LIST OF FIGURES

Page

1. INTRODUCTION

Optical methods of thermometry and magnetometry have been used for decades to explore interesting phenomena in a biological setting. In particular, optical thermometry has seen many developments over the years aimed at producing high accuracy biocompatible thermometers for use in research and clinical settings. Minimally invasive thermometers such as fiber-optic gallium-arsenide (GaAs) [1] and radiation thermometers [2-4] have been used in medicine to test for and control hyperthermia and hypothermia since the early 1980s. MRI compatible fiber-optic Bragg grating thermometers, developed in the late 1990s [5], have been used to measure the temperature of tissues in the pancreas and other organs undergoing laser ablation with high resolution [6-7]. Fluoroptic sensors employing fluorescence decay time resolved thermometry [8-9] have also shown promising applications in high resolution tissue temperature diagnostics during MRI guided laser ablation [10]. Non-invasive optical thermometry techniques primarily involve forward looking infrared (FLIR) imaging, which has demonstrated the ability to thermally discriminate between skin cancer lesions and healthy tissue [11].

Optical magnetometry has also been of critical importance in the drive for detailed study of biomagnetic fields. Atomic vapor magnetometers are one technology at the forefront of this effort. They possess extreme magnetic field sensitivity and have been a valuable tool in the field of high resolution spatially-resolved magnetocardiography [12-15].

The negatively charged nitrogen—vacancy (NV) center in diamond has been known for 40 years to possess unique quantum mechanical properties [16-17] which have been an invaluable tool for both magnetometry and thermometry in a diverse array of experimental settings. An NV center in diamond is formed when two adjacent diamond-lattice carbons are replaced with a nitrogen atom and a lattice vacancy occupied by a trapped electron. This system possesses optically addressable spin-state transitions whose fluorescence amplitude is sensitive to the magnetic field and temperature environment in which the nitrogen—vacancy diamond (NVD) resides.

NVD thermometers possess superior performance compared to other industry standard optical thermometry techniques [1-11, 18], with accuracies exceeding 20 mK and response times in the K/ms range [19-20].

With AC magnetic field sensitivities better than 3 $\mathrm{fT}/\sqrt{\mathrm{Hz}}$ [21] and DC field sensitivities of up to 60 $\mathrm{pT}/\sqrt{\mathrm{Hz}}$ [22], NVD magnetometers have sensitivities that are competitive with state of the art superconducting quantum interference devices (SQUID) [23] and atomic vapor magnetometers [24]. The solid-state, biocompatible form-factor of the NVD provides a potential for miniaturization that can engender high-sensitivity, ultra-high spatial resolution magnetic field and magnetic gradient imaging in a platform suitable for diagnostics in an *in vivo* setting [22, 25-29].

The objective of this dissertation is to demonstrate dual use monolithic fiber-optic NVD sensors capable of high-sensitivity, high-resolution magnetometry and fast, high-accuracy thermometry amenable to *in vivo* biological environments.

The structure of this dissertation reflects the design evolution of fiber-optic NVD probes towards the goal of *in vivo* bio-sensing of spatial temperature distributions and magnetic fields under the supervision of Professor Aleksei Zheltikov at Texas A&M University.

The first part (section 2) is devoted to the design, fabrication, testing, and implementation of fiber-optic NVD thermometer probe technology with up to 30 μm spatial resolution and better than 100 mK accuracy suitable for *in situ* cellular thermometry.

The second part (section 3) is devoted to the design evolution, demonstration, and application of fiber-optic NVD magnetogradiometer probes with sensitivities on the order of 100 $\mathrm{nT}/\sqrt{\mathrm{Hz}}$ and spatial resolutions of up to 6 μm for future use in the characterization of biomagnetic fields.

2. FIBER-OPTIC THERMOMETRY WITH NITROGEN—VACANCY CENTERS IN DIAMOND[*]

Modern optics offers a vast arsenal of tools for temperature measurements under hostile conditions and in remote sensing arrangements. Coherent Raman spectroscopy [30] is widely used for thermometry of combustion, flames, and plasmas, [31-32] enabling a remote online monitoring and diagnostics of internal combustion engines and flames in reaction chambers. Fiber-optic sensors provide indispensable instruments for temperature measurements in harsh and corrosive environments and for medical diagnostics using magnetic resonance imaging and nuclear magnetic resonance systems [33-34]. The temperature sensitivity of magnetic-resonance spectra of NV centers in diamond [35] has enabled new regimes of optical thermometry, allowing temperature measurements with a milli-kelvin accuracy and nanometer-scale spatial resolution [36], thus offering a unique tool for a thermometry of living cells [37]. By coupling a NVD to an optical fiber with an integrated microwave transmission line, it is possible to create a compact, monolithic probe simultaneously capable of optical thermometry and magnetometry [19, 38] that is ideal for use in *in vivo* thermometry.

[*] Parts of this section are reprinted with permission from, "Fiber-based thermometry using optically detected magnetic resonance" by I. V. Fedotov, S. Blakley, E. E. Serebryannikov, N. A. Safronov, V. L. Velichansky, M. O. Scully, and A. M. Zheltikov [19] and adapted from, "Fiber-optic control and thermometry of single-cell thermosensation logic" by I.V. Fedotov, N.A. Safronov, Yu.G. Ermakova, M.E. Matlashov, D.A. Sidorov-Biryukov, A.B. Fedotov, V.V. Belousov, and A.M. Zheltikov [37]. The work adapted from ref. [37] is copyrighted under the Creative Commons Attribution 4.0 International license (https://creativecommons.org/licenses/by/4.0/)

2.1 THERMOMETRY WITH NITROGEN—VACANCY CENTERS IN DIAMOND

In the early 90s [39], the energy level structure of the NV center was determined to possess a fluorescent dipole transition whose $m_s = \pm 1$ spin-triplet excited state sublevels selectively couple via an inter-system crossing and a low amplitude fluorescent infrared (IR) singlet-singlet dipole transition to an intermediate metastable singlet state. The metastable singlet state itself couples to the $m_s = 0$ triplet ground state sublevel via a second inter-system crossing, creating a mechanism for transferring population between the $m_s = \pm 1$ and $m_s = 0$ ground state sublevels without contributing to the triplet-state transition fluorescence amplitude (Fig. 2.1 (a)) [19].

This decay path decreases overall fluorescence intensity of the NV center by as much as 20% for transitions involving the $m_s = \pm 1$ sublevels, thereby providing optical means for interrogating the NV center's spin state. By exciting the NV center with green laser excitation and applying microwave radiation with frequency targeted at the Zeeman induced level splitting between the $m_s = 0$ and $m_s = \pm 1$ sublevels, one can exploit the spin-state fluorescence contrast to create a plot of the fluorescence intensity versus applied microwave frequency, known as an ODMR spectrum [38]. The ODMR spectrum contains information on the temperature of the NVD and the sensitivity of the probe to temperature. In the absence of external magnetic fields, the $m_s = 0$ and $m_s = \pm 1$ states are split by $\boldsymbol{\Omega}_S \approx 2.87$ GHz (Fig. 2.1 (a)). This resonance is observed as a well resolved feature in the photoluminescence intensity I_{PL} measured as a function of the microwave frequency $\boldsymbol{\Omega}$. Even in the absence of external magnetic fields, a local strain

removes the degeneracy of this resonance, giving rise to two well-resolved features in $I_{PL}(\Omega)$ ODMR spectra (Fig. 2.1 (b)). As the temperature of diamond increases, this profile of the zero-external-magnetic-field resonance is shifted toward lower microwave frequencies at a rate of approximately -75 kHz/K. In these experiments, this method of thermometry is implemented in a fiber format.

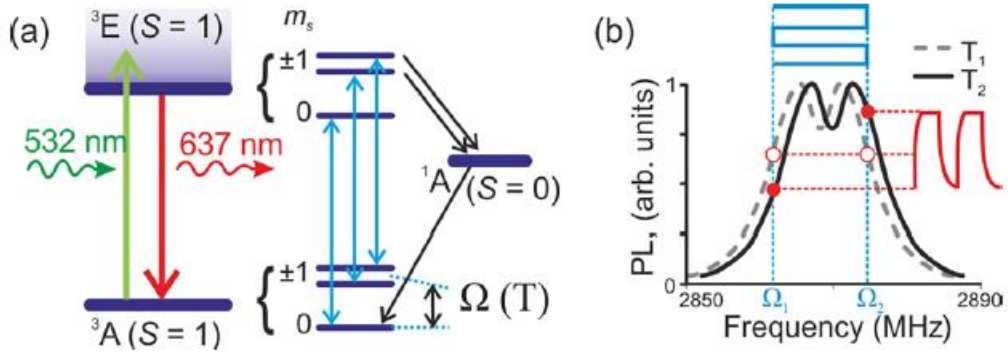

Fig. 2.1 (a) Diagram of energy levels of NV^- centers with a temperature-dependent splitting $\Omega(T)$ of the $m_s = 0$ and $m_s = \pm 1$ states in the spin-triplet ground state. Optical excitation and photoluminescence processes are also shown. (b) Zero-field magnetic-resonance spectra measured for two different temperatures $T_1 > T_2$. The blue line shows a rectangular modulation of the microwave frequency. The red line shows the differential photoluminescence signal.

2.2 FABRICATION OF NITROGEN—VACANCY DIAMOND PLATFORM FIBER-OPTIC THERMOMETERS

The fiber-optic NVD thermometers demonstrated in the following sections were fabricated in a three stage process that involves attachment of the NVD to a cleaved fiber tip with an optically transparent adhesive (Fig. 2.2 (a)-(b)), followed by the incorporation of a two-wire microwave transmission line by first forming a wire loop around and then affixing the remainder of the two-wire transmission line to the optical fiber body with another adhesive (Fig. 2.2 (c)-(d)).

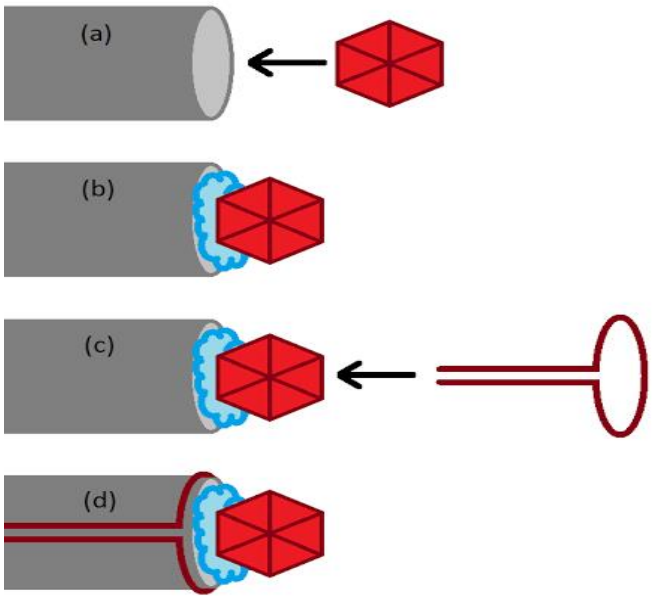

Fig. 2.2 (a) A diamond is placed on the tip of the fiber, (b) diamond is affixed to fiber tip with an optical adhesive, (c) two wire transmission line is bent into a loop in preparation for attachment to fiber, (d) two-wire transmission line is affixed to fiber body with loop wrapped around fiber tip.

The first step in this process (Fig. 2.2 (a)) was accomplished by first stripping the desired optical-fiber of its polymer jacket using a razor blade. Additional sonication in an acetone solution for 5 minutes may be necessary depending on the tenacity of the plastic jacket. An NVD is placed on a glass microscope in a microscope, and the optical fiber is taped down to the microscope stage so that the tip of the fiber is immobile with respect to the movements of the microscope slide containing the diamond. The fiber tip is brought in proximity to the diamond by translating the position of the microscope slide using the microscope's built-in translation stage.

The second step (Fig. 2.2 (b)) is performed by applying a drop of optical adhesive to the tip of the optical fiber using a needle. The diamond is then moved onto the fiber tip using the microscope translation stage. This glue is allowed to dry before the next step is performed.

The third step (Fig. 2.2 (c)) involves bending a straight segment of wire into the shape of a loop by wrapping it around the head of a needle whose outer diameter approximately that of the outer diameter of the optical fiber. Straight segments of the wire that will run along the body of the fiber are bent from the wire loop using the pointed tip of the needle, so as to form a 90 degree angle with the plane of the wire loop.

The fourth step (Fig. 2.2 (d)) involves attaching the newly manufactured microwave transmission line to the fiber body using an optical adhesive.

2.3 FIBER-BASED THERMOMETRY USING OPTICALLY DETECTED MAGNETIC RESONANCE

In this section, it is demonstrated that recently developed fiber-optic probes coupled with NV centers in diamond and integrated with a microwave transmission line can enable fiber-format optical thermometry with an accuracy of 0.02 K and spatial resolution limited by the size of a diamond crystal attached to the tip of an optical fiber. The electron spin of NV centers in a diamond microcrystal attached to the tip of this fiber probe is manipulated by a frequency-modulated (FM) microwave field and is initialized by laser radiation transmitted through the optical tract of the fiber probe. The photoluminescence (PL) spin-readout return from NV centers is captured and delivered by the same optical fiber [38,40], allowing the spatial temperature profiles to be mapped with a high speed and high sensitivity by applying a properly optimized differential lock-in detection technique.

To demonstrate fiber-based thermometry, a compact probe that integrates an optical fiber, an NV-diamond quantum sensor, and a microwave transmission line is used [25, 38]. For the NV-diamond sensor, high-pressure high-temperature commercial diamond microcrystals were used. These diamond microcrystals were enriched with NV defects by irradiation with mega-electron volt (MeV) electrons on an accelerator and annealing at a high temperature, yielding a density of NV centers up to 10^{16} cm^{-3}. A diamond microcrystal with a diameter of 250 μm was attached (Fig. 2.3) to the tip of an optical fiber with a core diameter of 200 μm and a numerical aperture NA ≈ 0.2 with a

mechanical manipulator under an optical microscope and fixed on the fiber tip with ethyl cyanoacrylate glue.

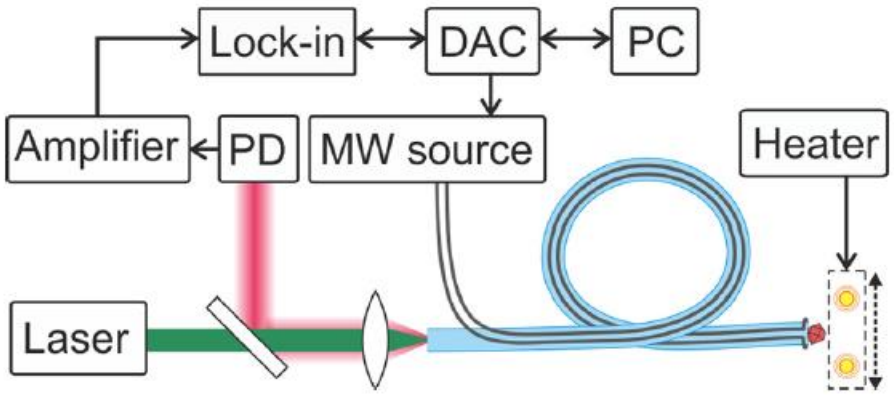

Fig. 2.3 Diagram of the experimental setup: PD, photodetector; DAC, digital-to-analog converter; PC, computer.

The electron spin of the ground-state triplet of NV centers is manipulated by this sensor through the electron spin resonance with a microwave field, which is delivered to the diamond microcrystal with NV centers through a two-wire transmission line, running along the optical fiber (Fig. 2.3) and consisting of a pair of copper wires 50 μm in diameter each. The two-wire transmission line is short-circuited with a loop, winding around the fiber tip (Fig. 2.3) and inducing a microwave field distribution with a maximum at the location of diamond microcrystal.

Optical polarization and initialization of NV centers in diamond are provided by the 5 mW, 532 nm second-harmonic output of a compact cw Nd:YAG laser, which is delivered to the diamond microcrystal on the fiber tip through the 200 μm diameter core of the fiber probe (Fig. 2.3), and is transmitted through this fiber to the detection system, consisting of a silicon photodiode, a low-noise preamplifier, and a lock-in amplifier (Fig. 2.3).

For high-speed, high-sensitivity temperature measurements, the electron spin of NV centers is manipulated in these experiments with a FM microwave field (Fig. 2.1 (b)), following the method of real-time magnetic-field sensing earlier demonstrated by Schoenfeld and Harneit [41]. In this scheme, a compact voltage-controlled oscillator (VCO) delivers a microwave field within a frequency range from 2.3 to 3.1 GHz with a power of 5 dBm and a linewidth of less than 1 kHz. A programmable digital-to-analog converter is used to apply a rectangular frequency modulation to the VCO output [blue line in Fig. 2.1 (b)], $\Omega(t) = \Omega_{\mathrm{m}} + \Delta$ for $n/\nu_{\mathrm{m}} < t < (n + 1/2)/\nu_{\mathrm{m}}$and $\Omega(t) = \Omega_{\mathrm{m}} - \Delta$ for$(n + 1/2)/\nu_{\mathrm{m}} < t < (n + 1)/\nu$, where Ω_{m} is the central frequency of the microwave field, Δ is the amplitude of frequency modulation, ν_{m} is the frequency modulation rate, and n is an integer.

The central frequency of the FM microwave field Ω_{m} is chosen in such a way as to coincide with the central frequency Ω_{s} of zero-field magnetic resonance at T_{z} = 306 K. The modulation frequency is set at $\nu_{\mathrm{m}} \approx 1330$ Hz. Modulation at the same frequency is also applied to a reference signal used for lock-in detection. With the amplitude of frequency modulation chosen equal to $\Delta \approx 5.5$ MHz, the difference between the PL

signals I_{PL} $(\Omega_1 = \Omega_m - \Delta)$ and I_{PL} $(\Omega_2 = \Omega_m + \Delta)$ at T_z is zero [dashed curve in Fig. 2.1 (b)]. As the magnetic resonance is shifted in response to temperature variations, the lock-in amplifier delivers a signal (red line, Fig. 2.1 (b)) proportional to the difference of PL intensities at the frequencies $\Omega_m \pm \Delta$ (solid curve, Fig. 2.1 (b)).

The diamond microcrystal on the fiber tip is heated by 532-nm laser radiation delivered through the optical tract of the fiber (Fig. 2.3). The increase in the laser power *P* delivered to the diamond microcrystal shifts the zero-field magnetic resonance in the $I_{PL}(\Omega)$ spectra toward lower microwave frequencies (Figs. 2.4 (a)-(b)), indicating a heating of diamond and allowing the temperature of diamond to be retrieved from the spectral shift of the zero-field magnetic resonance (Fig. 2.4 (c)).

Moreover, within a broad range of laser powers (up to 40 mW in Figs. 2.4 (a)-(b)), the frequency shift of the zero-field magnetic resonance and, hence, the temperature of diamond retrieved from this shift are accurately fitted with a linear function of the laser power. Within this range of laser powers, the central frequency of the zero-field magnetic resonance Ω_s is also accurately fitted by a linear function of temperature *T* with $d\Omega_s/dT \approx 74$ kHz/K (Fig. 2.4 (c)), which agrees well with the results of earlier studies. [36]

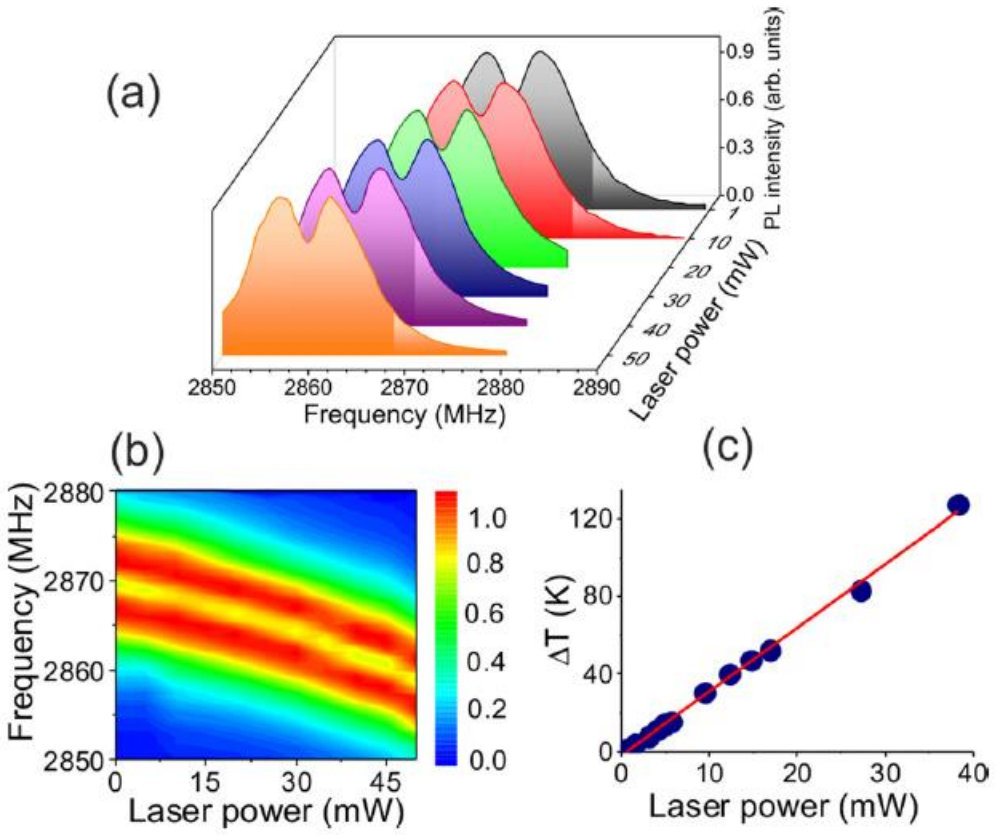

Fig. 2.4 (a) Intensity of photoluminescence from NV centers in a diamond microcrystal attached to the fiber tip measured as a function of the frequency of the microwave field delivered to the fiber tip through the microwave transmission line for different laser powers. (b) Zero-field magnetic-resonance profiles measured as a function of the laser power. (c) The temperature of a diamond microcrystal on the fiber tip retrieved from the shift of the zero-field magnetic resonance as a function of the laser power.

The validity of this calibration of the NV-diamond fiber thermometer was verified within a broad range of temperatures through a series of test experiments reproducing canonical cases of standard heat conduction theory, based on the heat conduction equation $c_p \rho \, \partial T/\partial t = \alpha r^{-m} \, \partial (r^m \, \partial T/\partial r)/\partial r$, where c_p is the heat

capacity, ρ is the density, m = 1 for a cylindrically symmetric geometry and m = 2 for a spherically symmetric arrangement, $T = T(r, t)$ is the temperature, r is the cylindrical radial coordinate for m = 1 and the spherical radial coordinate in the case of m = 2, t is the time, and α is the thermal conductivity.

In the first experiment, the diamond microcrystal on the tip of the fiber was heated by laser radiation until a stationary level of the PL signal was achieved, whereupon laser radiation was switched off, and the temperature decrease of a cooling diamond was measured using the above-described experimental procedure. Results of these measurements are presented by dots in Fig. 2.5 (a). These measurements are analyzed by using the heat conduction equation with m = 2, r understood as the spherical radial coordinate, and a diamond microcrystal on the tip of the fiber approximated by a spherical particle with a typical radius $R_d \approx 150$ μm. This heat conduction equation is solved separately for diamond, with $\alpha_d \approx 2000$ W/(mK), $c_{p,d} \approx 500$ J/(kgK), and $\rho_d \approx 3500$ kg/m^3, air, with $\alpha_a \approx 0.026$ W/(mK), $c_{p,a} \approx 1005$ J/(kgK), and $\rho_a \approx 1.225$ kg/m^3, and silica (fiber material), with $\alpha_s \approx 1.38$ W/(mK), $c_{p,s} \approx 2052$ J/(kgK), and $\rho_s \approx 2200$ kg/m^3.

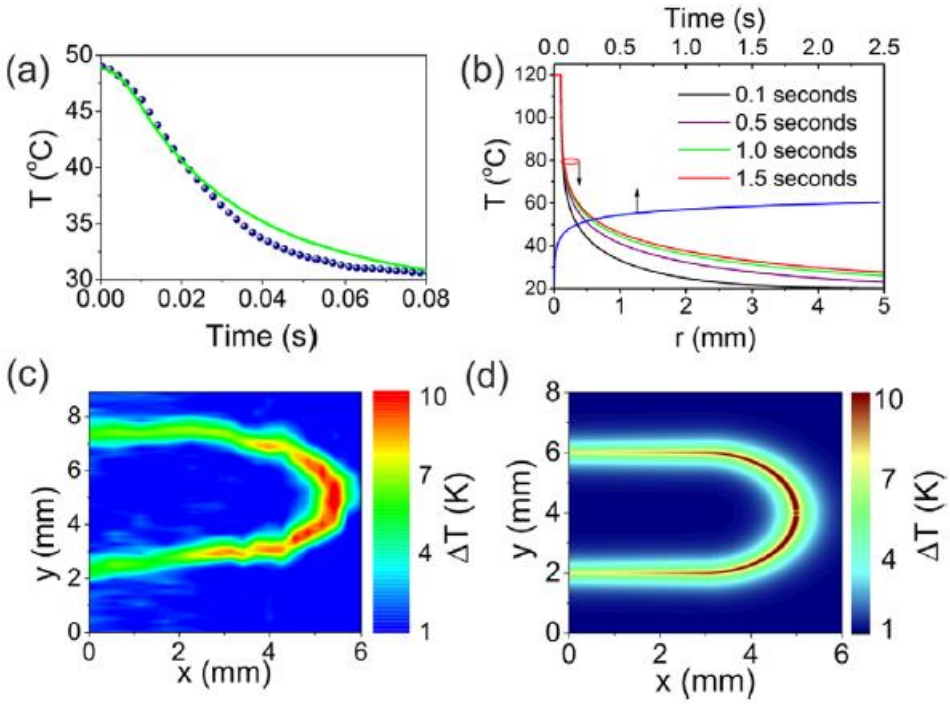

Fig. 2.5 (a) The temperature of the diamond microcrystal as a function of time: (circles) measurements performed with the use of the fiber thermometer, (solid line) solution of the heat-conduction equation. (b) Heat-conduction equation analysis of the evolution of the temperature gradient off a heated copper wire in the air: the temperature of the air at a distance of 300 μm from the wire (blue line) and temperature gradients 0.1 s (black line), 0.5 s (purple line), 1.0 s (green line), and 1.5 s (red line) following the turn-on of the heater. (c) and (d) Maps of temperature distribution around the copper wire (c) calculated by solving the heat-conduction equation and (d) measured with the NV-diamond fiber thermometer.

Since the thermal conductivity of silica in the fiber is much higher than that of air, the cooling of laser-heated diamond occurs predominantly through the diamond–silica interface. The solutions to the heat conduction equation in diamond and silica should meet the fourth-kind boundary conditions, dictated by the experimental geometry, requiring the equality of temperatures and heat fluxes on the surface of the

diamond microcrystal. Solution to the heat conduction equation, as can be seen from Fig. 2.5 (a), provides an accurate fit for the experimental results, reproducing a rapid decrease in the temperature of the diamond microparticle on the fiber tip to the steady-state temperature on a subsecond time scale.

In a second experiment, the NV-diamond fiber thermometer was used to measure a temperature distribution at a certain distance from a copper wire with a radius $R_0 \approx 0.1$ mm, heated by a temperature-controlled soldering iron. The heated wire was mounted on a three-dimensional translation stage and scanned relative to the fiber probe. Results of these measurements were analyzed by solving the heat conduction equation in the cylindrical geometry, with $m = 1$ and r understood as the cylindrical radial coordinate, for the air. Since the thermal conductivity of copper (≈ 400 W/(mK)) is much higher than the thermal conductivity of atmospheric air, the heat conduction equation is solved for atmospheric air with the first type boundary condition defined on the surface of the metal wire, $T(R_0, \mathrm{t}) = T_0$, where T_0 is the temperature of the wire, which is kept constant by an external heat source. For the conditions of these experiments, T_0 was set to approximately 390 K.

Heat conduction equation analysis shows that the temperature gradient induced by the copper wire in the experimental setup reaches its steady-state profile on a time scale of about 1 s (Fig. 2.5(b)). The map of the steady-state temperature distribution measured along the copper wire is shown in Fig. 2.5(c). The temperature profile predicted by the heat conduction equation agrees very well with experimental measurements (cf. Figs. 2.5 (c)-(d)). Since the plane of the heated wire is tilted with

respect to the plane of scanning by 1.2°, the separation between the fiber probe and the metal wire increases as the fiber probe is scanned from the center of the wire to its ends. As a result, the temperature measured by the fiber probe lowers. This tendency is also is in full agreement with the heat conduction equation analysis.

In a separate experiment, the stability of temperature measurements was studied as a function of the integration time τ of the lock-in amplifier. In these experiments, the diamond microcrystal on the tip of the fiber was irradiated by laser light with a constant peak power, helping to keep diamond at a constant temperature, $T_0 \approx 296$ K. Temperature measurements with an integration time $\tau = 1$ s yield a trace (Fig. 2.6 (a)) with a typical standard deviation $\sigma \approx 0.06$ K (dashed line, Fig. 2.6 (a)), which sets a limit on the accuracy of temperature measurements. Increasing the integration time up to $\tau =$ 10 s helps to reduce fluctuations on experimental temperature traces (Fig. 2.6 (b)), lowering the standard deviation of temperature measurements down to $\sigma \approx 0.02$ K (dashed line, Fig. 2.6 (b)).

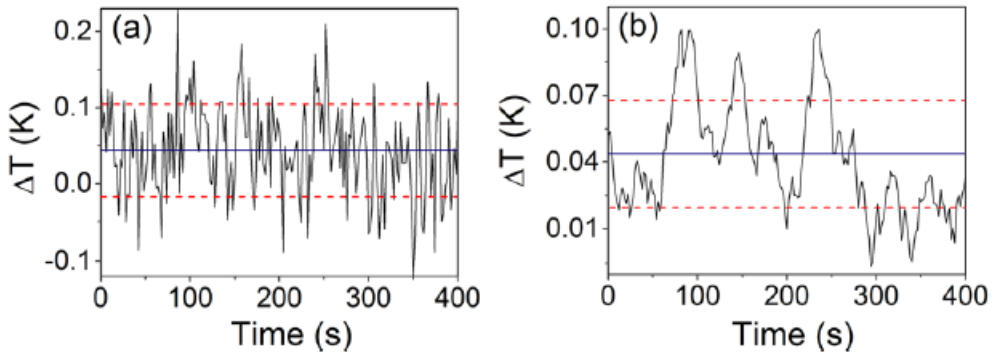

Fig. 2.6 Variations of temperature readings from the NV-diamond fiber thermometer with time with an integration time of the lock-in amplifier set equal to τ = 1 s (a) and 10 s (b). Dashed lines show the standard deviation σ.

To summarize, this section has shown that fiber-optic probes coupled with NV centers in diamond and integrated with a microwave transmission line enable fiber-format optical thermometry with a spatial resolution limited by the size of the diamond crystal attached to the tip of an optical fiber. Temperature measurements with an accuracy of 0.02 K have been performed by combining this NV-diamond fiber thermometer with a properly optimized differential lock-in detection technique. Due to the unique combination of a high accuracy and high spatial resolution, the fiber thermometer developed in this work offers a powerful tool for on-line temperature measurements in hostile environments and *in vivo* monitoring of heat-related contrasts in biological systems.

2.4 FIBER-OPTIC THERMOGENETICS

In this section, a literature review of work by Professor Aleksei Zheltikov's group at Moscow State University covering the application of the fiber probes discussed in section 2.3 to problems in thermogenetics is presented [37]. This work is summarized below.

Optogenetic methods have been employed to select and modulate light sensitive channels expressed in genetically modified cells in a spatially precise manner [42-48], offering the opportunity to study phenomena that control memory, learning, and cognition at a cellular level. Thermogenetics offers a complementary control regime to that of optogenetics by employing ion channels sensitive to thermal modulation that are robustly active even at low levels of gene expression [49-59]. In order to realize the potential of optogenetics, a biocompatible probe is needed that is capable of simultaneously delivering a precisely controlled thermal stimulus and accurately measuring the temperature of a cell under study with high spatial resolution. The compact NVD fiber probes described in section 2.3 are particularly well suited for application to thermogenetics.

The group at Moscow State University prepared the test environment used to demonstrate the feasibility of fiber-optic thermogenetics by transfecting Human Embryonic Kidney 293 (HEK-293) cells with vectors expressing the G-GECO 1.2 calcium indicator [60] and a thermally sensitive TRPA1 calcium channel [55].

The HEK-293 cells were cultured in a petri dish according to guidelines established in [61]. In previous work, cells under study were heated using the microwave radiation emanating from the microwave transmission line around the tip of the fiber-optic NVD thermometer probes presented in section 2.3 [62].

In the present work, microwave power is deliberately kept low in order to avoid unintended heating of nearby cells. Instead, laser heating of the diamond microcrystal on the tip of a fiber NVD thermometer is used to increase the temperature of a nearby HEK-293 cell beyond the thermal activation threshold of the TRPA1 calcium channel.

The channel opens once the activation temperature has been reached and allows calcium to flow into the cell, thus activating the G-GECO1.2 calcium indicator and causing it to fluoresce when exposed to 473 nm light (Fig. 2.6).

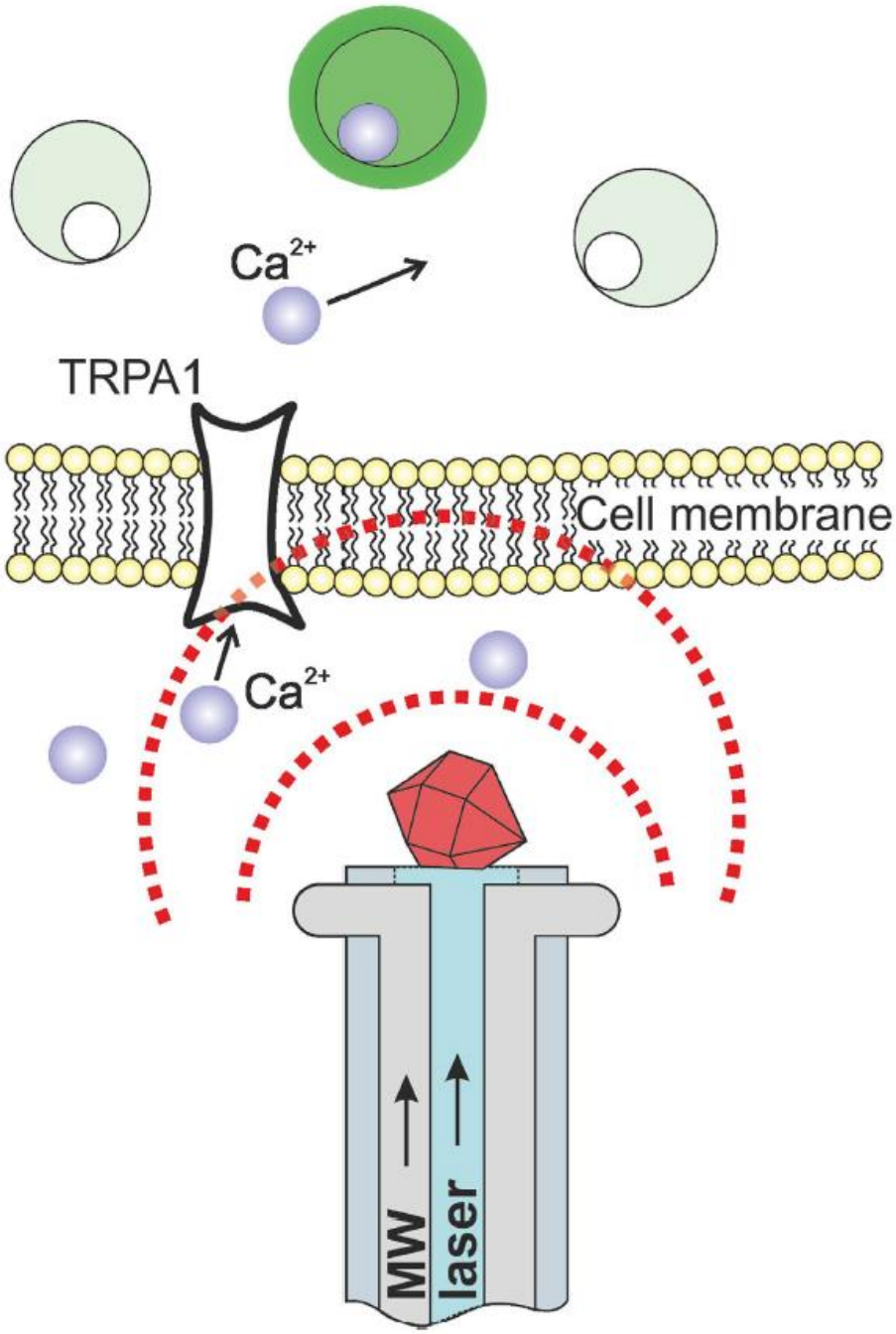

Fig. 2.6 Laser heating of the diamond induces a localized temperature distribution around the cell. When the temperature is increased to a level higher than that of the TRP channel activation threshold, Ca^{2+} ions flow through the TRP channel, causing the G-GECO 1.2 Ca^{2+} indicator to emit green fluoresce in the presence of 473 nm laser excitation. Adapted with permission from [37].

The petri dish was placed on a translation stage and imaged with a microscope system capable of delivering the 473 nm laser excitation and collecting the signal fluorescence from the G-GECO 1.2 calcium indicator.

The laser-heated tip of an NVD fiber-optic thermometer was placed in the petri-dish and the temperature was increased in a stepwise fashion. The temperature increase of each step was allowed to diffuse in a radial fashion throughout the petri-dish for 100 seconds, and a second fiber-optic NVD thermometer connected to the ODMR detection setup described in section 2.3 was used to measure the temperature at a grid of points in the petri-dish using the lock-in detection technique described in refs. [25,41] (Fig. 2.7).

The fluorescence of the cells under study was recorded at each temperature step (Fig. 2.8 (a)) in order to determine the activation temperature of each cell (Fig. 2.8 (b)-(c)).

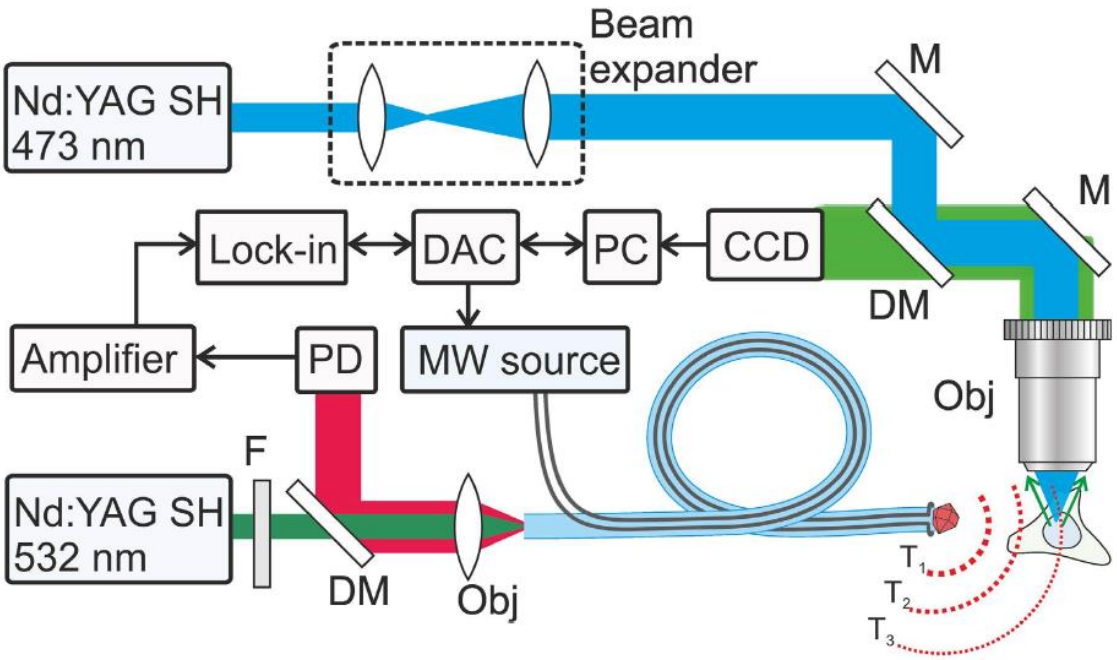

Fig. 2.7 The experimental setup used to demonstrate fiber-optic thermogenetic manipulation of HEK-293 cells. The ODMR signal acquisition system consists of a coupling objective (Obj), a dichroic mirror (DM), a photodiode (PD), a signal pre-amplifier, a lock-in amplifier referenced to a modulated microwave source (MW source), and a digital acquisition card (ADC) connected to a personal computer (PC). 473 nm laser excitation from the second harmonic of a Neodymium YAG laser (Nd:YAG SH) is focused onto the sample using an objective. The fluorescence of the cells under study was imaged with a microscope onto a CCD camera through a dichroic mirror. The spherical temperature distribution (T_1, T_2, T_3) induced by laser-heating the diamond probe tip was characterized using a second NVD fiber-thermometer to measure temperature at various points in a grid-fashion across the petri dish. Adapted with permission from [37].

In Fig. 2.8 (a), the fluorescence intensity of a group of nine HEK-293 cells is recorded by the CCD camera at four laser power settings, corresponding to four different diamond temperatures. As the temperature increases with each higher laser power

setting, measurable changes in the fluorescence intensity of the cells in closest proximity to the heat source are detected between panel 1 in Fig 2.8 (a) and panel 2 in Fig 2.8 (a).

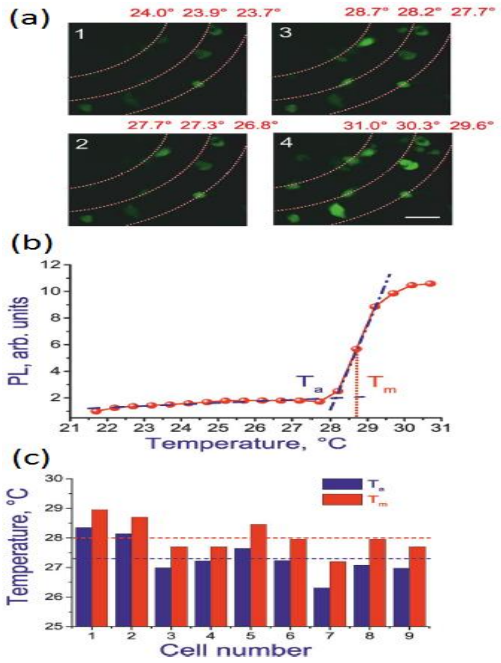

Fig. 2.8 (a) Images of cells under study taken using CCD camera for 532 nm excitation powers $P_0 \approx 18$ mW (panel 1), 56 mW (panel 2), 68 mW (panel 3), and 88 mW (panel 4). The scale bar [bottom right, panel 4] is 50 μm. The laser-heated fiber NVD thermometer tip is located in the top left corner of each image at a distance of 325 μm above the plane of the images. Red concentric dotted lines denote isotherms emanating from the NVD heat source. Temperature values for these isotherms measured with a second NVD sensor are indicated in red above the images. (b) The G-GECO 1.2 fluorescence intensity is plotted as a function of measured temperature for one cell in the field of view of the microscope. Dashed lines correspond to the background fluorescence level at temperatures beneath the activation threshold. The dash—dotted line describes a linear fit to the rising segment of the G-GECO 1.2 fluorescence intensity for temperatures near to and beyond the activation threshold. The point of intersection for these lines defines the activation threshold T_a of the cell. (c) Activation thresholds T_a (blue) and T_m (red) for the nine cells under study. Dashed lines denote mean values of these thresholds. Adapted with permission from [37].

Cells further from the heat source begin to fluoresce more intensely (panels 3 and 4, Fig. 2.8 (a)) with higher laser powers, indicating that the activation temperature of these more distant cells has been reached. In Fig. 2.8 (b), the activation temperature of a single cell in the petri dish was measured from a plot of fluorescence amplitude versus temperature. The activation threshold temperature T_a of this cell was determined by finding the intercept between the average background fluorescence level at a temperature beneath the activation threshold (blue dashed line, Fig. 2.8 (b)) and the linear fit line to the rising edge of the fluorescence curve for temperatures beyond the activation threshold (blue dashed-dotted line, Fig. 2.8 (b)), where T_m denotes the median temperature point of the slope in the activation threshold curve. At temperatures more than 1°C beyond the activation threshold, the TRP channel is fully open and the fluorescence signal begins to saturate (signal at T > 29°C, Fig. 2.8 (b)). This technique was used to determine the activation temperatures for the remaining eight cells in the field of view of the microscope (Fig. 2.8 (c)). The average values and standard deviations for T_a and T_m for the nine cells under study were $T_a \approx 27.3 \pm 0.6$ °C and $T_m \approx 28.0 \pm 0.5$ °C. The standard deviation in activation temperatures not only describes measurement errors innate to the fiber NVD thermometer probes, but also captures the innate variations in threshold temperature for TRP channels between each cell. This provides insight into the extent to which collections of cells can be thermally controlled as a whole. To summarize this section, thermogenetic activation of individual cells has been demonstrated and characterized using the fiber-optic NVD thermometers developed in section 2.3.

3. FIBER-OPTIC MAGNETIC GRADIOMETRY WITH NITROGEN—VACANCY CENTERS IN DIAMOND*

NV centers in diamond [63–67] offer unique opportunities for high-sensitivity magnetic-field measurements at room temperature with unprecedented spatial resolution [26, 28-29] and potentially attainable sensitivities [21] comparable to those of SQUID magnetometers. While the highest sensitivities of NV-diamond-based magnetic-field sensing and gradiometry have been achieved using confocal microscopy [36], optical fibers have been recently shown [19, 25, 38] to offer a missing link for a practical implementation of NV-diamond-based sensing in a variety of environments, including magnetic-field and temperature measurements in biological systems. In real-life applications, weak magnetic fields from objects under study, e.g., a beating heart or firing neurons, need to be detected against a strong, noisy background due to the magnetic field of the Earth or technogenic environment. Atomic coherent effects in alkali-metal vapors have been shown to enable the creation of innovative ultrahigh-sensitivity magnetic gradiometers [13-14], allowing the magnetic field of the heart to be mapped with a high accuracy from outside the body [14-15]. The limited spatial resolution of this technique motives the search for an all-solid-state design of a highly sensitive biocompatible optical magnetometer for use in an *in vivo* environment.

* Parts of this section are reprinted with permission from "Room-temperature magnetic gradiometry with fiber-coupled nitrogen—vacancy centers in diamond" by S. M. Blakley, I.V. Fedotov, S. Ya. Kilin, and A.M. Zheltikov [22] and from "Fiber-optic vectorial magnetic-field gradiometry by a spatiotemporal differential optical detection of magnetic resonance in nitrogen—vacancy centers in diamond" by S. M. Blakley, I.V. Fedotov, L. V. Amitonova, E. E. Serebryannikov, H. Perez, S. Ya. Kilin, and A.M. Zheltikov [27]

3.1 MAGNETOMETRY AND GRADIOMETRY WITH NITROGEN—VACANCY CENTERS

The presence of a magnetic field in the environment around the NV center induces energy level splitting of the $m_s = \pm 1$ ground-state sublevels as a function of the projection of the field magnitude along the NV center axis. NV centers oriented in the direction of the local magnetic field couple more strongly, thus inducing a larger Zeeman splitting in the sublevels. It is therefore possible to determine the direction and magnitude of an unknown local magnetic field by comparing the separation of the frequency values of successive pairs of ODMR peaks from their zero-field values. The frequency values associated with these peaks can be found by fitting the peaks in the PL spectrum with a Lorentzian function.

To determine the magnitude and direction of the magnetic field from the ODMR spectrum, the Hamiltonian for this system must first be solved: [28]

$$\widehat{H} = \frac{\mu_B g}{h}\mathbf{BS} + D\left[S_Z^2 - \frac{S(S+1)}{3}\right] + E(S_X^2 - S_Y^2) \tag{3.1}$$

In the expression for the Hamiltonian, B is the magnetic field to be measured, μ_B is the Bohr magneton, g is the Landé g-factor ($g \approx 2$ for the electron), D and E are system dependent frequency parameters, and S_j (j=X, Y, Z) is the spin-state projection on the various spatial axes. Solving the Hamiltonian yields a third order characteristic equation [28]:

$$x^3 - \left(\frac{D}{3} + E^2 + \beta^2\right)x - \frac{\beta^2}{2}\Delta - \frac{D}{6}(4E^2 + \beta^2) + \frac{2D^3}{27} = 0 \tag{3.2}$$

The parameters of the characteristic equation are defined as: $\beta = \frac{\mu_B g B}{h}$, and for D >> E, $\Delta \cong D\cos 2\theta_i$, where θ_i is the polar angle between the quantization axis of the i^{th} (i = 1,2,3,4) NV center and the magnetic field respectively (Fig. 3.1). Solving the characteristic equation results in equations describing the magnetic field magnitude and direction as a function of the frequency value of the location parameter of the Gaussian fit [28]:

$$B = \sqrt{\frac{h^2}{3\mu_B^2 g^2}(\Omega_{1i}^2 + \Omega_{2i}^2 - \Omega_{1i}\Omega_{2i} - D^2 - 3E^2)} \tag{3.3}$$

$$\begin{aligned}\cos 2\theta_i \cong & \frac{7D^3 + 2(\Omega_{1i} + \Omega_{2i})[2(\Omega_{1i}^2 + \Omega_{2i}^2) - 5\Omega_{1i}\Omega_{2i} - 9E^2]}{9D(\Omega_{1i}^2 + \Omega_{2i}^2 - \Omega_{1i}\Omega_{2i} - D^2 - 3E^2)} \\ & + \frac{-3D(\Omega_{1i}^2 + \Omega_{2i}^2 - \Omega_{1i}\Omega_{2i} + 9E^2)}{9D(\Omega_{1i}^2 + \Omega_{2i}^2 - \Omega_{1i}\Omega_{2i} - D^2 - 3E^2)}\end{aligned} \tag{3.4}$$

In Eqs. 3.3-3.4, Ω_{1i} and Ω_{2i} are the frequencies of the peaks in the PL spectra corresponding to the i^{th} NV orientation axis in the diamond lattice. The angles θ_i also obey the identity:

$$\sum_{i=1}^{4} \cos\theta_i = 0 \tag{3.5}$$

The projection of the magnetic field onto the four NV quantization axes yields expressions for the angle between B and each quantization axis as a function of the polar (θ) and azimuthal (φ) angles of B with respect to the z-axis of the NVD lattice frame (Fig. 3.1):

$$\left.\begin{aligned} \cos\theta_1 &= \cos\frac{\alpha}{2}\sin\theta\sin\varphi - \sin\frac{\alpha}{2}\cos\theta \\ \cos\theta_2 &= \cos\frac{\alpha}{2}\sin\theta\sin\varphi + \sin\frac{\alpha}{2}\cos\theta \\ \cos\theta_3 &= -\sin\frac{\alpha}{2}\sin\theta\cos\varphi - \cos\frac{\alpha}{2}\sin\theta\sin\varphi \\ \cos\theta_4 &= \sin\frac{\alpha}{2}\sin\theta\cos\varphi - \cos\frac{\alpha}{2}\sin\theta\sin\varphi \end{aligned}\right\} \tag{3.6}$$

Solving for θ and φ as a function of θ_i yields:

$$\left.\begin{aligned} \theta &= \cos^{-1}\left(\frac{\cos\theta_1 - \cos\theta_2}{2\sin\frac{\alpha}{2}}\right) \\ \varphi &= \sin^{-1}\left(\frac{\cos\theta_1 + \cos\theta_2}{2\cos\frac{\alpha}{2}\sin\theta}\right) \end{aligned}\right\} \tag{3.7}$$

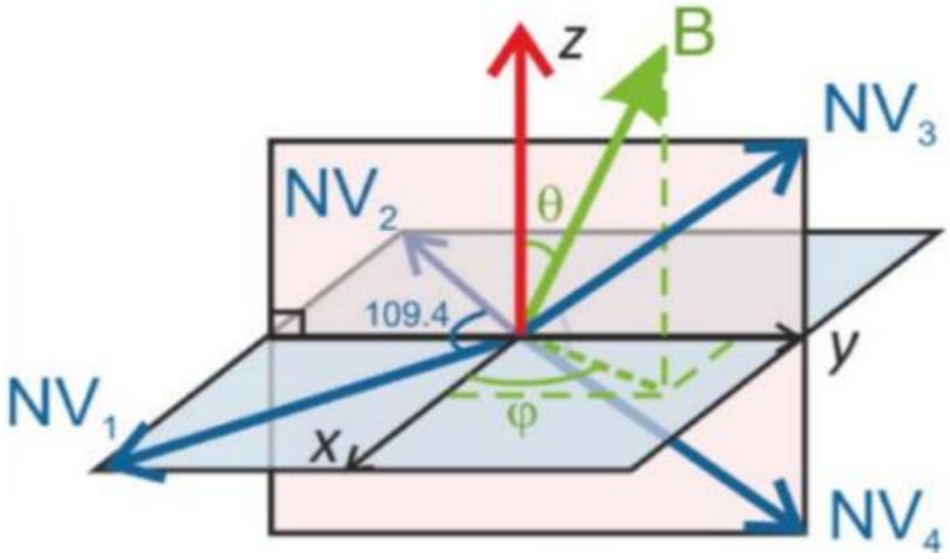

Fig. 3.1 Local coordinate frame of NV centers in diamond lattice. Blue arrows represent quantization axes of NV centers (i = 1, 2, 3, 4) in the tetragonal diamond lattice separated by an angle $\alpha \approx 109.4°$. Red arrow represents z-axis of local coordinate frame. Green arrow represents direction of local magnetic field, where θ is the polar angle displacement of B from z-axis and φ is the azimuthal displacement from the x-axis of the projection of B into the x-y plane.

In order to determine the experimental magnetic field sensitivity, the approximation E << D is used in Eq. 3.3 to determine that $\Omega_{1i} - D = D - \Omega_{2i}$, and thus that $\Omega_{2i} = 2D - \Omega_1$. This result is substituted into Eq. 3.3 to yield:

$$B \approx \frac{h}{\mu_B g}\sqrt{(D - \Omega_{1i})^2 - E^2} \tag{3.8}$$

Eq. 3.8 is Taylor expanded to first order around small variations in Ω_{1i}, called $\delta\omega$, to yield the expression for the limit of experimental magnetic field sensitivity:

$$\Delta B \approx \frac{h}{\mu_B g}\delta\omega\left[\frac{D - \Omega_{1i}}{\sqrt{(D - \Omega_{1i})^2 - E^2}}\right] \tag{3.9}$$

As long as $\delta\omega << E$, Eq. 3.9 is a valid approximation to the experimental magnetic field sensitivity. Applying the earlier approximation E << D to Eq. 3.9, the equation for sensitivity as a function of frequency shift $\delta\omega$ becomes:

$$\Delta B \approx \frac{h}{\mu_B g}\delta\omega \tag{3.10}$$

When a magnetic field is measured at two points in space it is possible to calculate the magnetic field gradient between the two points (henceforth known as field gradient or gradient). When a scalar gradient measurement is desired, it is sufficient to divide the difference between the two field magnitudes at the two measurement points by the spatial separation between the two measurement points:

$$|\nabla B| = \frac{|\overrightarrow{B_1}| - |\overrightarrow{B_2}|}{d} \tag{3.11}$$

In Eq. 3.11, B_i refers to the magnetic field at i^{th} point in space and d refers to the distance between points i and i+1.

A vector gradient can be calculated approximately by taking finite differences between components of the two vectors of interest, forming a rank 2 tensor whose elements obey the following relation:

$$\overrightarrow{\nabla B} = \overrightarrow{\overrightarrow{G}} = \delta_{jk} \frac{\Delta B_i}{dx_j} \overrightarrow{e_i}\, \overrightarrow{e_k} \tag{3.12}$$

The repeated indicies (i, j, and k each with values of 1, 2, and 3) in Eq. 3.12 obey the rules of Einstein summation notation. δ_{jk} represents the Kronecker delta function on indicies j and k, ΔB_i is the difference between the i^{th} component of the two vectors $\overrightarrow{B_1}$ and $\overrightarrow{B_2}$, dx_j is the distance between the two measurement points in the i^{th} coordinate axis (e.g. $dx_1 = dx$, $dx_2 = dy$, and $dx_3 = dz$), and $\overrightarrow{e_k}$ is the unit vector along the k^{th} coordinate axis.

In order to calculate gradient of a vector in all three coordinate axes in the matrix $\overrightarrow{\overrightarrow{G}}$, magnetic vector measurements must be made at four points spanning all three coordinate axes. This property generalizes to n-dimensions, where n+1 magnetic vector measurements are required to calculate the vector gradient in n-dimensions.

The differential nature of the gradient measurement has the feature that it excludes any contribution of field components that are approximately constant with respect to the order of the gradient, e.g. a first order gradient will cancel effects of field components that are approximately constant in space: if $B_{Tot} = B_0(x) + B_{Signal}(x)$, where B_0 is a bias field with the property that it varies by less than the magnetic field sensitivity (δB) (and are thus indistinguishable from noise) over the distance between measurement points x_1 and x_2, and B_{Signal} is the field of interest that varies by more than

δB over the region of interest, then $\nabla B_{Tot} = (B_0(x_1) - B_0(x_2) + B_{Signal}(x_1) - B_{Signal}(x_2))/(x_1 - x_2) = \nabla B_{Signal}$. In this way, a gradiometer is capable of measuring weak, spatially localized fields in the presence of arbitrarily strong spatially homogeneous bias fields provided that the near field of the object under study changes by more than the magnetic field sensitivity over the minimum spatial resolution.

The fundamental limit of a magnetic gradiometer's spatial resolution is defined as the distance between two measurements at which the field varies by exactly the sensitivity of the magnetometer. Thus the fundamental resolution limit is constrained by both δB and the field profile as a function of distance; e.g. if the field difference (ΔB) is equal to δB over a distance of 1 μm, then the limit of resolution is 1 μm. The real resolution (δr) of each gradient measurement is limited by these two factors and one additional factor: the smallest distance between measurement points (Δr) that the system can make. If the field varies by δB over a distance larger than Δr, then $\delta r > \Delta r$. If the field varies by the sensitivity over a distance smaller than the minimum distance between measurements, then $\delta r = \Delta r$.

3.2 FABRICATION OF NITROGEN—VACANCY DIAMOND FIBER-OPTIC MAGNETIC GRADIOMETER PROBES

The fiber-optic magnetic gradiometer probes demonstrated in the following sections were fabricated in two different regimes. The first fabrication regime involves the creation of a dual-fiber NVD gradiometer, used in sections 3.3 and 3.4. This was accomplished by applying an optical adhesive to the tip of a cleaved 200 μm diameter optical fiber and using a three-axis translation stage to adjust the position of each fiber until it was in the correct position on the diamond. As a result, two parallel fibers with a core-to-core separation of 480 μm were affixed to a 1 mm diameter bulk NVD crystal (Fig. 3.2 (a)). The second fabrication regime involves the creation of a dual-core photonic crystal fiber (PCF) NVD gradiometer using a dual-core PCF with 4 μm core-to-core separation (Fig. 3.2 (b)-(c)). This was accomplished by manipulating a glass slide bearing a ~40 μm diamond microcrystal onto the surface of the cleaved tip of the PCF using a three-axis translation stage so that the diamond bridged both cores. Once the diamond bonded with the fiber tip via electrostatic forces, two different techniques were attempted to form a permanent bond between the fiber tip and the NVD. The first technique involved applying a drop of optical adhesive to the fiber-NVD junction with a needle. This technique proved to be inadequate because surface tension of the optical adhesive would pull the NVD off of the core region. Thus a second technique was developed that involved evaporating the optical adhesive located on a sheet of metal underneath the fiber-NVD junction with a heating element. This allowed the adhesive to

build up in the junction over the course of several minutes forming a permanent bond between the two. The gradual buildup of the adhesive prevented a drop from forming on the tip, thus avoiding the problem of surface tension pulling the diamond off of the core region.

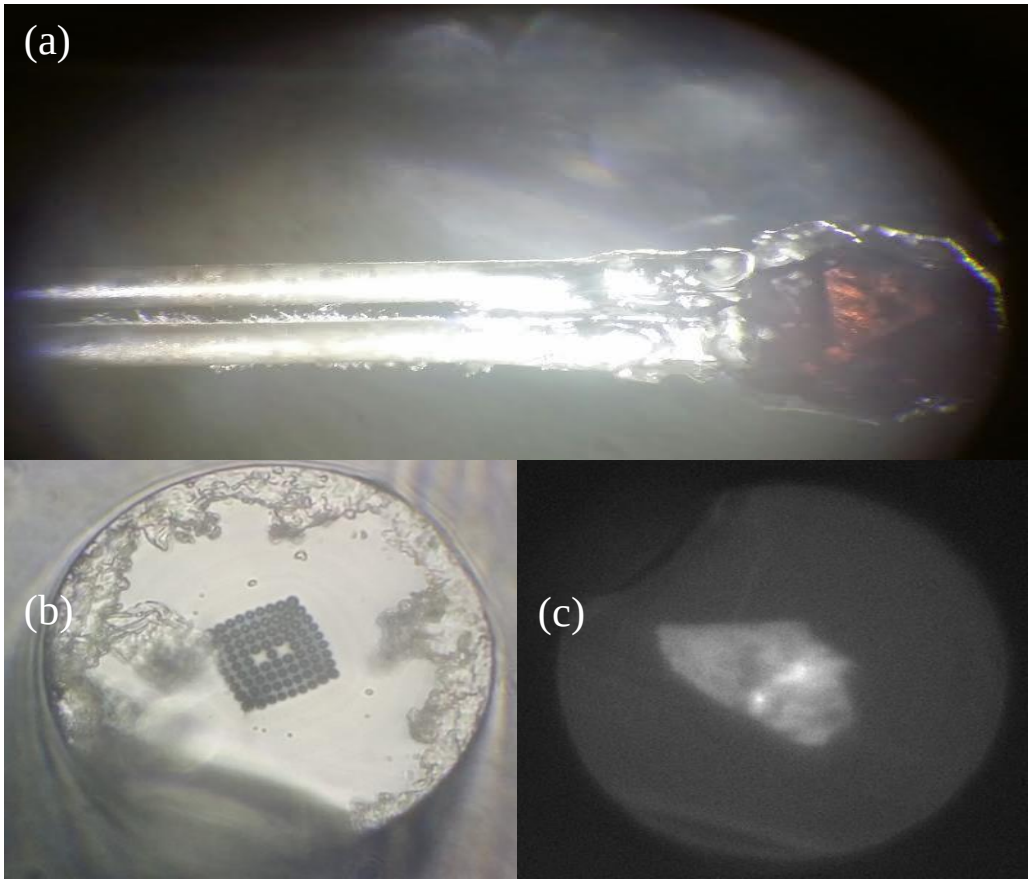

Fig. 3.2 (a) Dual-fiber NVD probe fabricated by affixing two parallel 200 μm diameter optical fibers to a single 1 mm NVD crystal at a core-to-core separation of 480 μm. (b) The dual-core PCF used to fabricate the dual-core PCF gradiometer probe. The cladding of this fiber consists of a 9 by 9 grid of air holes with two holes replaced with solid glass in the 5th row at columns 4 and 6. (c) A ~40 μm diamond microcrystal affixed to the fiber surface bridging the two cores with an optical adhesive. Laser excitation illuminates the diamond in the two regions covering the core.

3.3 ROOM-TEMPERATURE MAGNETIC GRADIOMETRY WITH FIBER-COUPLED NITROGEN—VACANCY CENTERS IN DIAMOND

In this section, a versatile high-spatial-resolution solid-state magnetic gradiometer that operates on a fiber platform using the optically detected magnetic resonance in NV centers of diamond is demonstrated. An ultracompact design of this fiber-based magnetic gradiometer is achieved by integrating an NV-diamond magnetic sensor with a two-fiber opto-microwave interface, which couples NV centers to microwave and optical fields, used to resonantly drive and interrogate the spin of NV centers. This fiber-based magnetic gradiometer is shown to provide a spatial resolution below 0.5 mm and a magnetic-field sensitivity at the level of 60 $pT/Hz^{1/2}$.

The fiber-optic magnetic gradiometer developed in this work consists of a bulk NV-center-enriched diamond particle, a pair of optical fibers attached to this diamond particle at two different locations, and a two-wire transmission line for the delivery of the microwave field. Two identical optical fibers, each having a core diameter of 200 μm, are attached, using a mechanical manipulator, to an NV-diamond particle with a diameter of about 1 mm (Fig. 3.3). The fibers are fixed to the NV-diamond sensor with a core-to-core separation $d \approx 480$ μm (Fig. 3.4 (a)).

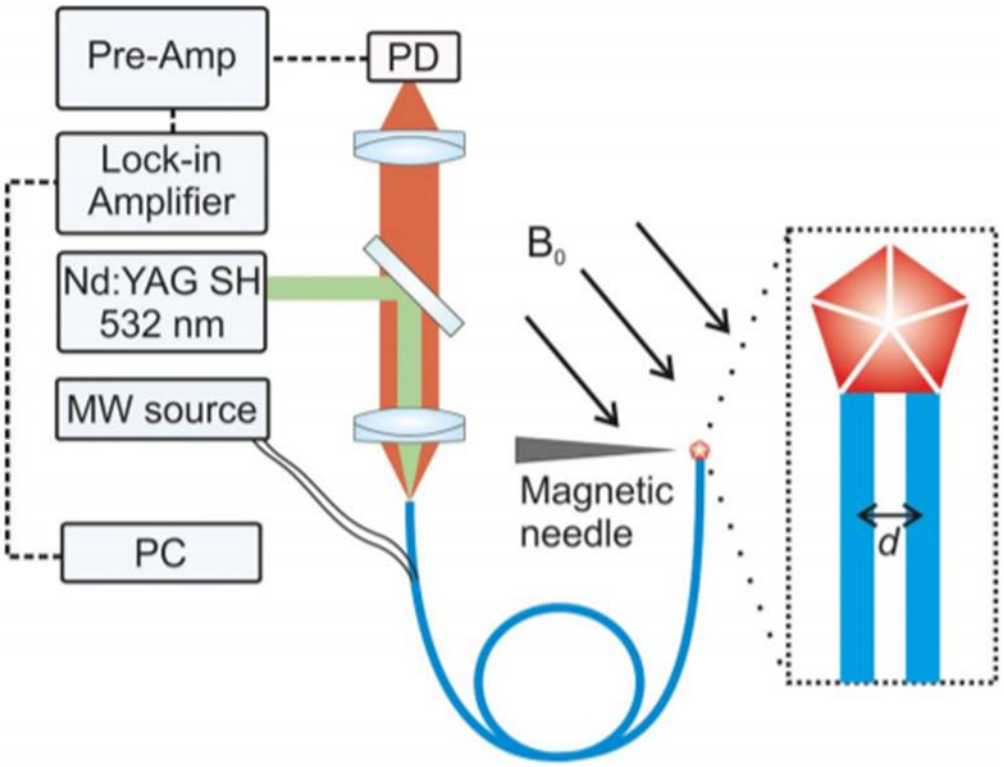

Fig. 3.3 Experimental setup: Nd:YAG SH, continuous-wave Nd:YAG laser with second-harmonic output; MW source, microwave source; PC, personal computer; PD, photodetector.

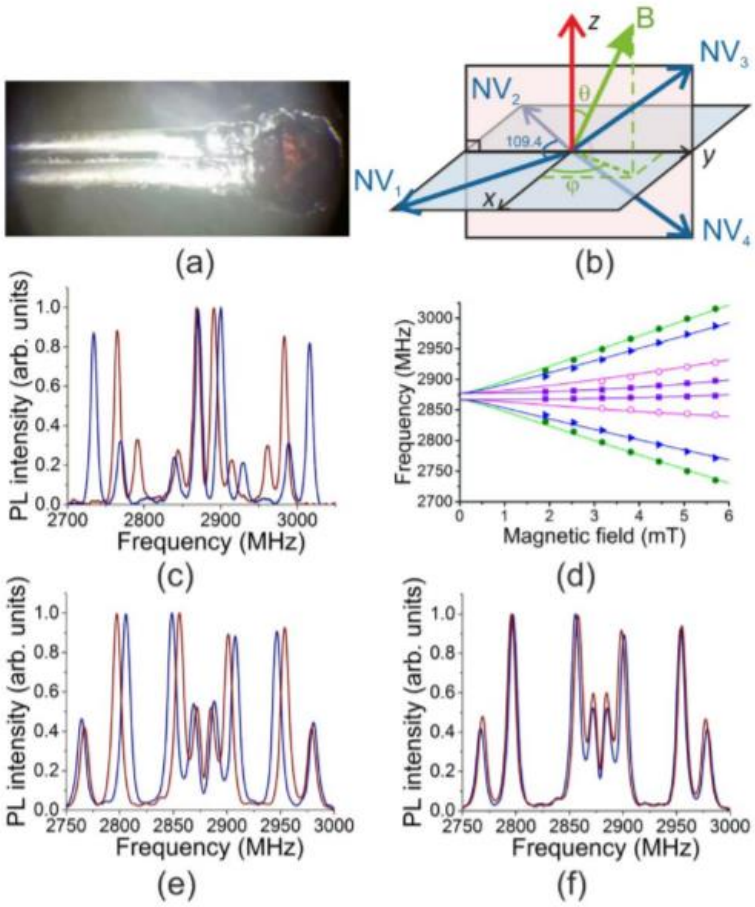

Fig. 3.4 (a) A fiber-based magnetic gradiometer integrating an NV diamond sensor with a two-fiber opto–microwave interface. (b) An external magnetic field B versus the x-, y-, and z-coordinate axes related to the crystal lattice of diamond, with NV axes 1 and 2 lying in the xy-plane, the z-axis perpendicular to this plane, and the y-axis chosen along the bisector of the angle between NV axes 3 and 4 and belonging to the plane defined by these axes. (c) Typical ODMR spectra recorded through one of the two fiber channels of the fiber gradiometer in the presence of a homogeneous magnetic field $B_0 \approx 4.4$ mT (red line) and 5.7 mT (blue line). (d) The frequencies Ω_j (i=1, 2, 3, 4) of the four pairs of the Zeeman-shifted peaks in the ODMR spectra plotted as a function of the magnitude of the magnetic field: (data points) experimental results and (solid lines) calculations. (e) ODMR spectra recorded through the same fiber channel of the fiber gradiometer probe with the spatially inhomogeneous component of the magnetic field switched on (red line) and off (blue line) with $B_0 \approx 4.1$ mT. (f) ODMR spectra recorded through the first (blue line) and second (red line) fiber channels of the fiber gradiometer in the presence of an external magnetic field $B = B_0 + B_i$.

In experiments, the laser pump is delivered by the optical fibers to the NVD sensor. An acousto-optical modulator is used to couple 50 mW of the 532-nm second-harmonic output of a cw Nd:YAG laser into each of the optical fibers attached to the NVD sensor, thus providing a parallel optical excitation of NV centers at two different locations in diamond. The PL signal from NV centers is then collected by the same fibers, enabling differential ODMR measurements (Fig. 3.3). Each optical fiber is used to measure the PL signal from NV centers in diamond as a function of the frequency of the microwave field delivered through the two-wire transmission line, thus enabling a fiber-based differential optical detection of the magnetic resonance (ODMR) of NV centers. The gradient of an external magnetic field is then retrieved through a comparative analysis of ODMR spectra I_1 (Ω) and I_2 (Ω) recorded through the first and second optical fibers.

For high-speed, high-sensitivity differential ODMR measurements, a rectangular modulation with a frequency $f_m \approx 1.13$ kHz is applied to the frequency of the microwave voltage-controlled oscillator output using a digit-to-analog converter, controlled by homemade dedicated software. The frequency of the modulated microwave output changes periodically in a rectangular fashion from its minimum at 2.3 GHz to its maximum value scanned from 2.5 to 3.1 GHz. A lock-in amplifier is then used to retrieve a signal at $f_m \approx 1.13$ kHz from the overall PL return signal detected by a photodiode and boosted by a preamplifier, thus discriminating the modulated spin readout against the constant PL background. A 14-bit analog-to-digital converter (ADC) was used to digitize the results of measurements and analyze the recorded I (Ω) spectra.

Fig. 3.4 (c) presents typical ODMR spectra recorded through one of the two fiber channels of the fiber gradiometer in the presence of a homogeneous magnetic field B_0 induced by a homebuilt solenoid, made of a 25.4-mm-diameter iron cylinder wrapped with 187 turns of 20-gauge copper magnet wire. The magnetic field induced by this solenoid is controlled by varying the dc current through the copper wire up to a maximum of 3 A. The ODMR spectra exhibit four well-resolved peaks at the frequencies of magnetic resonance, Ω_j (j = 1, 2, 3, 4), corresponding to four possible orientations of NV centers relative to the lattice of diamond (Fig. 3.4 (b)). As the external magnetic field is increased by increasing the electric current through the solenoid, all these magnetic resonances are shifted toward higher frequencies. As can be seen from Fig. 3.4 (d), the frequencies Ω_i of the peaks in the ODMR spectra measured as functions of the external magnetic field B (data points in Fig. 3.4 (d)) agree very well with the magnetic-resonance frequencies Ω_i calculated by solving the characteristic equation for the Hamiltonian H_s (solid lines in Fig. 3.4 (d)), providing an accurate calibration curve for magnetic field measurements.

In the magnetic gradiometry mode, the fiber probe is employed to perform differential ODMR measurements in the presence of an external magnetic field consisting of a strong spatially homogeneous magnetic field $\mathbf{B}_0$ from the above-described solenoid and a weak spatially inhomogeneous magnetic field $\mathbf{B}_i$ induced by a magnetized 1-mm-diameter metal needle. Fig. 3.4 (e) contains a plot of ODMR spectra recorded through the same fiber of the fiber probe with the spatially inhomogeneous

component of the magnetic field switched on and off. The field $\mathbf{B}_i$ is seen to give rise to detectable changes in the ODMR spectra.

Fig. 3.4 (f) contains ODMR spectra I_1 (Ω) and I_2 (Ω) recorded through two fiber channels of the fiber gradiometer in the presence of an external magnetic field $\mathbf{B} = \mathbf{B}_0 + \mathbf{B}_i$. In this experiment, the fiber magnetometer is placed at a distance of about 1 cm from the tip of the magnetized needle and oriented in such a way that only the magnitude of the magnetic field, but not its direction, changes from one fiber channel to another. The magnitudes of the magnetic field retrieved from the I_1(Ω) and I_2(Ω) ODMR spectra presented in Fig. 3.4 (f) are $B_1 \approx 0.35$ mT and $B_2 \approx 0.41$ mT, corresponding to a magnetic field gradient $|\Delta B/d| \approx 0.12$ mT⁄mm.

Figs. 3.5 (a)–(d) display the results of experiments, where the fiber gradiometer was placed at a distance of 1–2 mm from the tip of the magnetized needle. In such an experimental arrangement, not only the magnitude, but also the direction of the magnetic field changes from one fiber channel of the fiber gradiometer to another. Measurements performed with and without the spatially homogeneous component of the magnetic field are shown by red and blue lines, respectively. The spatially inhomogeneous component of the magnetic field retrieved from the ODMR spectra is $B_i \approx 1.4$ mT, $\theta_i \approx 3.2°$, $\varphi_i \approx 50°$ (Figs. 3.5 (a),(c)) and $B_i \approx 1.1$ mT, $\theta_i \approx 80°$, $\varphi_i \approx 2.0°$ (Figs. 3.5 (b),(d)) for measurements performed through the first fiber channel and $B_i \approx 1.2$ mT, $\theta_i \approx 7.4°$, $\varphi_i \approx 67°$ (Figs. 3.5 (a),(c)) and $B_i \approx 1.3$ mT, $\theta_i \approx 60°$, $\varphi_i \approx 7.4°$ (Figs. 3.5 (b),(d)) when measured through the second fiber channel. The magnetic fields retrieved from the

ODMR spectra and the respective field gradients agree very well with the results of calculations for the magnetic field B induced in this experimental geometry.

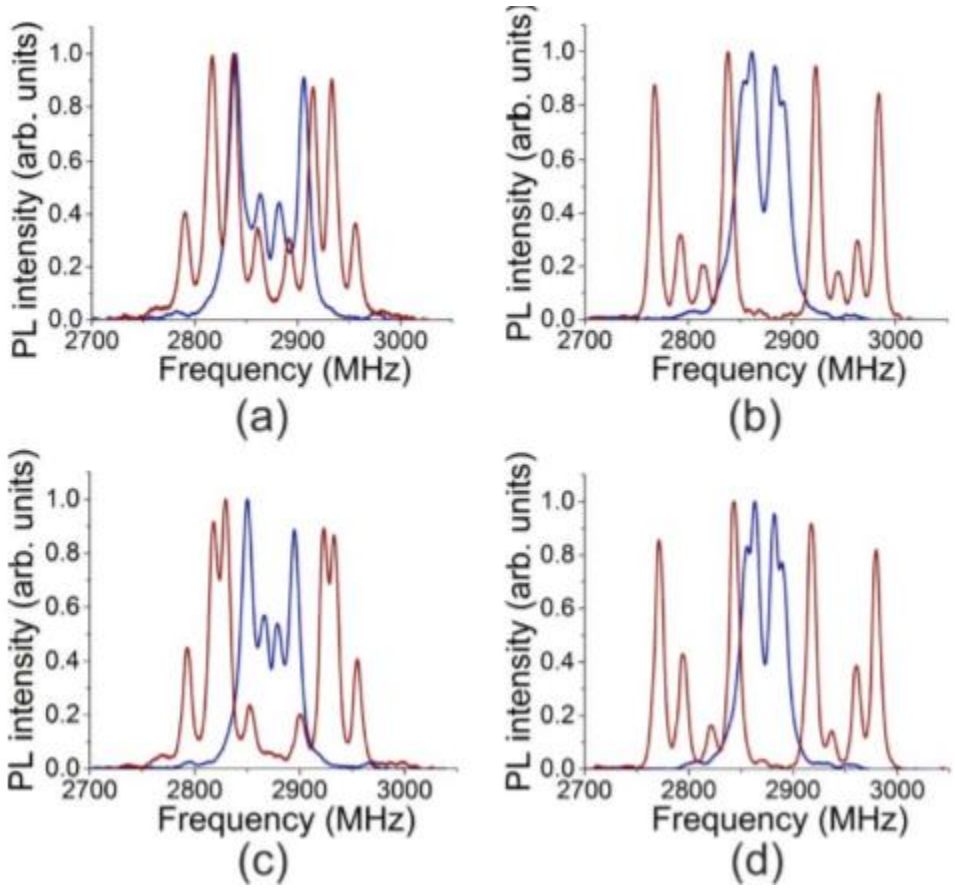

Fig. 3.5 ODMR spectra recorded through the first (a), (b) and second (c), (d) fiber channels of the fiber gradiometer in the presence of an external magnetic field $B= B_0+ B_i$ consisting of a spatially homogeneous component with $B_0 \approx 0$ (blue lines) and $B_0 \approx 4.4$ mT, $\theta_0 \approx 78°$, $\varphi_0 \approx 11°$ (red lines) and a spatially inhomogeneous component with $B_i \approx 1.4$ mT, $\theta_i \approx 3.2°$, $\varphi_i \approx 50°$ (a), (c) and $B_i \approx 1.1$ mT, $\theta_i \approx 80°$, $\varphi_i \approx 2.0°$ (b), (d) at the location of the first fiber channel.

The limiting sensitivity of magnetic-field detection provided by the fiber gradiometer demonstrated in these experiments is estimated as $\delta\eta = \sigma h \Delta\nu (C g \mu_B)^{-1} R^{-1/2}$ [68], where σ is the line shape factor, $\Delta\nu$ is the full width at half-maximum of the ODMR line, C is the ODMR contrast, and R is the PL photon count rate.

For the parameters of this system, $\sigma \approx 0.7$, $C \approx 0.05$, and $\Delta\nu \approx 8$ MHz, the sensitivity was found to be $\delta\eta \approx 60$ pT⁄Hz$^{1/2}$, assuming a laser power of 100 mW, the density of NV centers of $3 \cdot 10^{18}$ cm^{-3} , and the numerical aperture of the fiber channels $N \approx 0.4$.

At this level of sensitivity, the fundamental features of magnetocardiogram of a human heart, whose typical amplitude is about 100 pT, can be detected with an integration time τ of less than 1 s.

For the above-specified set of parameters, the lowest magnetic field gradient that can be detected using the fiber magnetic gradiometer demonstrated in this work, that is, with a spatial resolution of $d \approx 0.5$ mm and with $\tau \approx 1$ s $\delta B/d \approx 120$ pT⁄mm.

Even lower magnetic field gradients can be detected at a cost of spatial resolution. Specifically, in magnetocardiography of human heart, where a resolution of 5–6 mm would be adequate, magnetic field gradients as low as 10–12 pT⁄mm could be detected, offering an attractive alternative to magnetic gradiometers based on alkali metal vapor cells.

In summary, a versatile high-spatial-resolution solid-state magnetic gradiometer that operates on a fiber platform using the optically detected magnetic resonance in NV centers of diamond was demonstrated.

An ultracompact design of this fiber-based magnetic gradiometer is achieved by integrating an NV-diamond magnetic sensor with a two-fiber opto–microwave interface, which couples NV centers to microwave and optical fields, used to resonantly drive and interrogate the spin of NV centers.

This fiber-based magnetic gradiometer is shown to provide a spatial resolution below 0.5 mm and a magnetic-field sensitivity at the level of 60 $pT/Hz^{1/2}$.

The techniques and ideas developed in this section will be utilized in the following sections to develop a suitable biocompatible magnetic gradiometer probe.

3.4 FIBER-OPTIC VECTORIAL MAGNETIC-FIELD GRADIOMETRY BY A SPATIOTEMPORAL DIFFERENTIAL OPTICAL DETECTION OF MAGNETIC RESONANCE IN NITROGEN—VACANCY CENTERS IN DIAMOND

In this section, the two-fiber NV-diamond magnetometer scheme presented in section 3.3 [22] was used for highly sensitive room-temperature vectorial magnetic-field gradiometry. For the highest sensitivity and noise immunity, differential ODMR measurements in both space and time were implemented, with magnetic-field gradient measurements supplemented with differential ODMR signal detection in the time domain, allowing efficient cancellation of low-frequency magnetic-field fluctuations and providing a sensitivity of magnetogradiometry at the level of 10^{-7} $\mathrm{nT}/\left(\mathrm{nm\ Hz}^{1/2}\right)$.

ODMR measurements are performed (Fig. 3.6) with a fiber probe consisting of two fibers with a center-to-center separation of approximately 480 μm attached to an NV diamond particle 1 mm in diameter [22]. For the highest sensitivity of magnetic-field gradiometry, this two-fiber magnetometer is used in combination with a second reference fiber probe, where a single optical fiber is attached to an identical 1-mm-diameter NV-diamond (left, Fig. 3.6). Optical interrogation of NV centers in diamond was provided by a 50-mW, 532-nm second-harmonic output of a Nd: YAG laser. Magnetic-resonance excitation of the spin of NV centers was provided by a 3-W microwave field, which was delivered to the NV diamond particles via a two-wire microwave transmission line integrated into each of the fiber probes [38]. A homebuilt solenoid was used to induce a spatially homogeneous bias magnetic field. The bias

magnetic field induced by the solenoid, applied normally to the fiber axes, provided a comfortable peak separation in ODMR spectra, thus improving the precision of magnetic-field measurements, and served as a spatially homogeneous component of the magnetic field for magnetic-field gradient measurements.

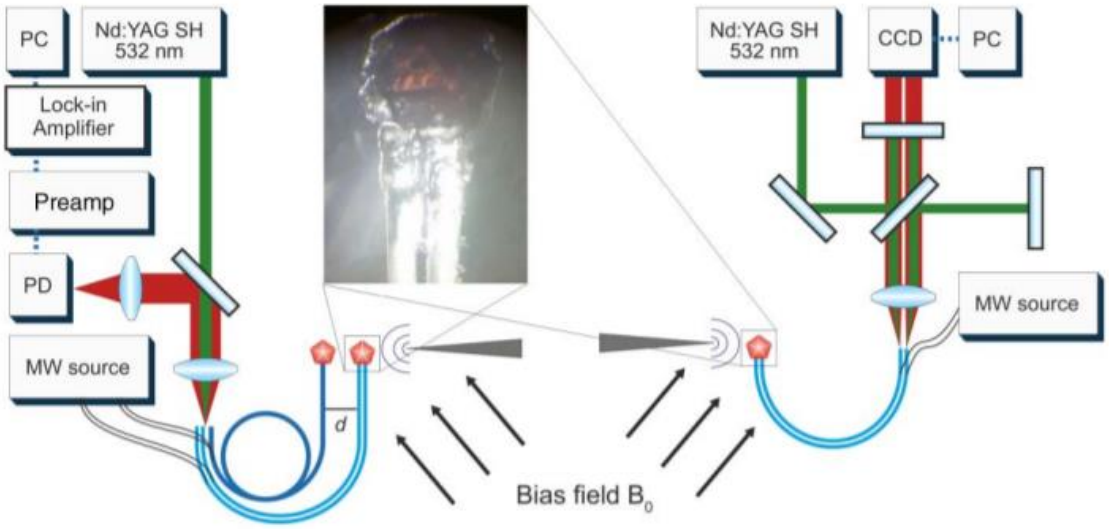

Fig. 3.6 Fiber-based magnetogradiometry: (left) the first modality, with two optical fibers attached to bulk NV-diamond magnetic-field sensors; (right) the second modality, with two optical fibers attached to a bulk NV-diamond magnetic-field sensor: Nd: YAG SH, Nd; YAG laser with a second-harmonic output; Preamp, preamplifier; MW source, microwave source; PD, photodetector. A microscope image of a two-fiber NV-diamond sensor is shown in the central part.

This experimental scheme enables two modalities of fiber-format ODMR measurements. In the first modality, ODMR measurements are performed using two spatially separated NV-diamond sensors coupled to optical fibers, as shown in the left

part of Fig. 3.6. In this experimental arrangement, the sensitivity of magnetic-field gradient measurements can be improved by increasing the distance between the fiber probes, albeit at the expense of the spatial resolution. The data acquisition system in this modality includes a photodiode for the detection of the PL signal, a preamplifier, a lock-in amplifier, and a 14-bit ADC. For a higher sensitivity of magnetic-field gradient measurements, the frequency of the microwave field applied to NV centers is modulated at 1 kHz, while the resulting electric signal is amplified by a preamplifier, digitized with a high-resolution ADC, and detected with a lock-in amplifier.

In the second modality, ODMR measurements are performed by simultaneously probing two sites an NV-diamond sensor through a two-fiber interface connected to the NV diamond sensor (right, Fig. 3.6). In this scheme, laser radiation is delivered by both fibers to optically interrogate simultaneously two sites in NV diamond. The PL signal is then delivered by the same fibers and is imaged onto a camera in real time. This modality provides a high spatial resolution and a high immunity to noise and temporal field fluctuations, which can be efficiently canceled by differential ODMR measurements in the time domain.

With the magnetic field read out in this field-sensing scheme simultaneously through two fibers, the results of these measurements are then used to compose a vector $\boldsymbol{G} = \left(\Delta B_x/\delta\,, \Delta B_y/\delta\,, \Delta B_z/\delta\right)$, where $\Delta B_i = B_i(\xi + \delta) - B_i(\xi)$, $B_i\,(\zeta)$ is the projection of the magnetic field $\boldsymbol{B}(\zeta)$ onto the ith coordinate axis $(i = x, y, z)$ read out at the point ζ, and δ is the separation of the two field readout points, defined by the distance between the fiber tips in the fiber probe. Reconstructing the full gradient of the magnetic

field [69] will then require two-point measurements with two other orthogonal orientations of the fiber gradiometer.

The sensitivity limit of magnetic-field measurements implemented in these experiments is determined by the frequency shift δω of a magnetic resonance that can still be reliably detected when measured against the instrumental noise. In this experiment, ODMR measurements are performed around the frequency ω_0 corresponding to the maximum steepness $\partial I_{PL}/\partial\omega$ of the magnetic-resonance contour $I_{PL}(\omega)$ [25]. The δω parameter can be defined as the change in the microwave frequency that shifts the noise trace of the PL signal by at least one standard deviation. A pair of typical noise traces of the PL signal from NV diamond measured through the reference fiber probe, where a single optical fiber is attached to a 1-mm-diameter NV-diamond sensor, is shown in Fig. 3.7 (a). The black trace in this figure corresponds to a microwave frequency of 2.861 GHz. The red trace is measured with the microwave frequency shifted by 1 kHz. The solid green and blue lines show the mean value of the PL signal for these traces. The standard deviation, shown by the dashed lines in Fig. 3.7 (a), is estimated as $\sigma \approx 35.7$ nT. The sensitivity of magnetic-field measurements determined from these measurements is $35.7\mathrm{nT}/\mathrm{Hz}^{1/2}$.

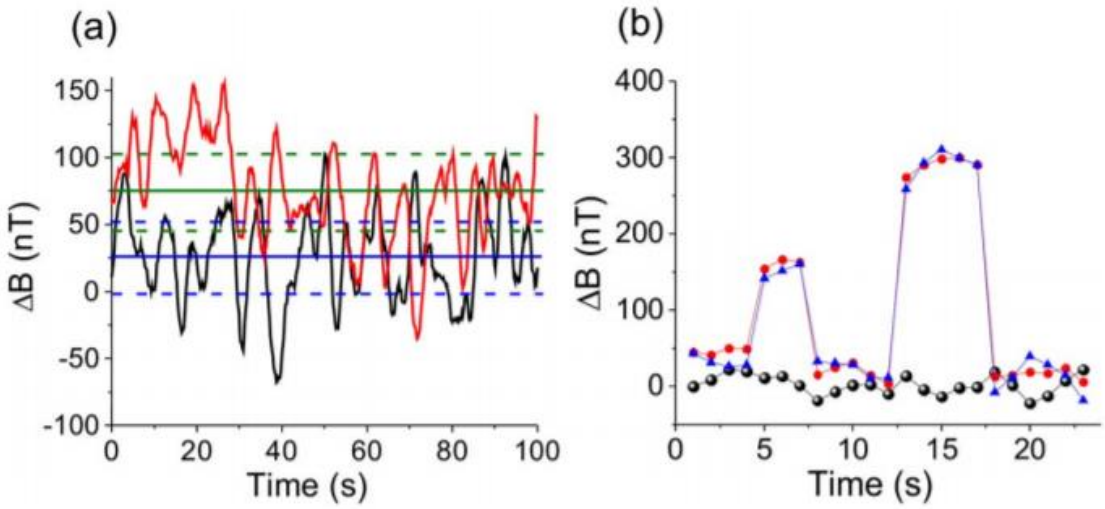

Fig. 3.7 (a) A pair of typical noise traces of the PL signal from the NV diamond measured through the reference fiber probe, where a single optical fiber is attached to a 1-mm-diameter NV-diamond sensor. The black trace corresponds to a microwave frequency of 2.861 GHz. The red trace is measured with the microwave frequency shifted by 1 kHz. The solid green and blue lines show the mean value of the PL signal for these traces. The standard deviation is shown by the dashed lines. (b) The PL traces recorded through the first (red) and second (blue) fibers of the two-fiber NV-diamond magnetogradiometer. The magnetic field is changed in a stepwise fashion at t= 5 s, 8 s, 13 s, and 17 s by varying the electric current through the solenoid. The trace of the differential signal is shown by the black line.

Experiments presented in Fig. 3.7 (b) demonstrate that unwanted variations in the magnetic field can be canceled in ODMR measurements performed with the two-fiber magnetic-field gradiometer (right, Fig. 3.6). In these experiments, variations in the external magnetic field are induced by varying the electric current through the solenoid. At t = 4 s, the current through the solenoid is increased by 0.1 A in a stepwise fashion and kept at a high level during 3 s, where upon the initial level of the electric current through the solenoid is restored. Within the time interval from 13 to 17 s, the electric

current is increased again, this time by 0.2 A. The traces of the PL signal measured through both fibers attached to the NV-diamond sensor (blue and red curves in Fig. 3.7 (b)) are seen to follow each other closely. The black curve in Fig. 3.7 (b) shows that variations in the magnetic field have been efficiently canceled in the differential signal. This experiment proves that high-frequency variations in the magnetic field are canceled in the differential signal delivered by the two-fiber NV-diamond magnetogradiometer, which reduces the overall noise and eventually improves the sensitivity of magnetic-field gradient measurements. A typical sensitivity of fiber-optic magnetogradiometry achieved with two fiber-coupled NV-diamond sensors separated by a distance of 5 cm in first-modality experiments is on the order of 10^{-7} $\mathrm{nT}/\left(\mathrm{nm\ Hz}^{1/2}\right)$.

In experiments presented in Figs. 3.8 (a)-(b), an NV-diamond sensor attached to two optical fibers is used for ODMR measurements on an inhomogeneous magnetic field induced by the magnetized needle with and without the solenoid-induced homogeneous bias field $B_0 \approx 2$ mT. The magnetic field gradients retrieved from the ODMR spectra recorded through the first and second fibers of the two-fiber probe in the presence (Fig. 3.8 (a)) and in the absence (Fig. 3.8 (b)) of the homogeneous bias magnetic field are 1.46 and 1.48 nT/nm, respectively. These results show that the background homogeneous magnetic field has been canceled in the differential signal with an accuracy of 0.02 nT/nm. The ability of this two-fiber NV-diamond sensor to detect steep profiles of weak, spatially inhomogeneous magnetic fields is demonstrated by experiments where a magnetized needle is used as a source of a rapidly decaying magnetic-field profile (Fig. 3.6). To illustrate the vectorial properties of the magnetic field and its gradient in such an

experimental arrangement, the magnetic field induced by a uniformly magnetized cylinder is calculated, whose diameter (0.5 mm) and length (3 cm) are taken in such a way as to match the sizes of the magnetized needle used in these experiments. In cylindrical coordinates ρ, φ and z, such a magnetic field has two nonzero components, $B_\rho = -\mu_0 \partial\Phi/\partial\rho$ and $B_z = -\mu_0 \partial\Phi/\partial z$, where Φ is the magnetic scalar potential, $\boldsymbol{B} = -\mu_0 \nabla \Phi$, and μ_0 is the vacuum permeability. Fig. 3.9 (a) contains a map of the vectorial properties of the magnetic field (arrows) and its magnitude $B = \left(B_\rho^2 + B_z^2\right)^{1/2}$ (color coding). As can be seen from this map, as well as from Fig. 3.9 (b), the field magnitude B rapidly decays with the distance $r = ((\rho - \rho_0)^2 + (z - z_0)^2)^{1/2}$ from the tip of the magnetized needle, located at a point with coordinates ρ_0 and z_0. Figs. 3.9 (c)-(d) show the behavior of the individual components of the magnetic field, B_ρ and B_z (solid lines), and the radial part of their gradients, $\partial B_\rho/\partial r$ and $\partial B_z/\partial r$ (dashed–dotted lines), calculated as functions of the distance r along the lines connecting the points where the field was measured in experiments with the tip of the magnetized needle (dashed lines, Fig. 3.9 (a)).

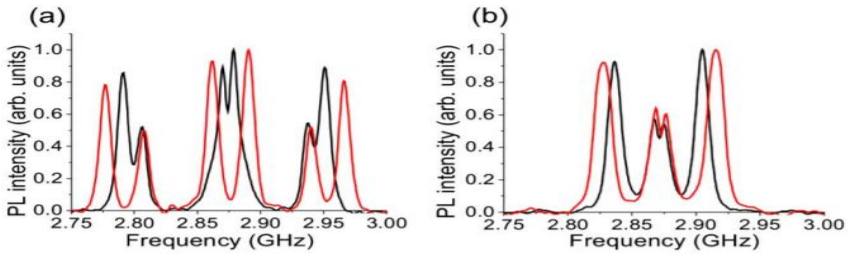

Fig. 3.8 Spectra of optically detected magnetic resonance measured through the first (red line) and second (black line) fibers of the two-fiber NV-diamond magnetogradiometer with (a) and without (b) a homogeneous bias magnetic field $B_0 \approx 2$ mT.

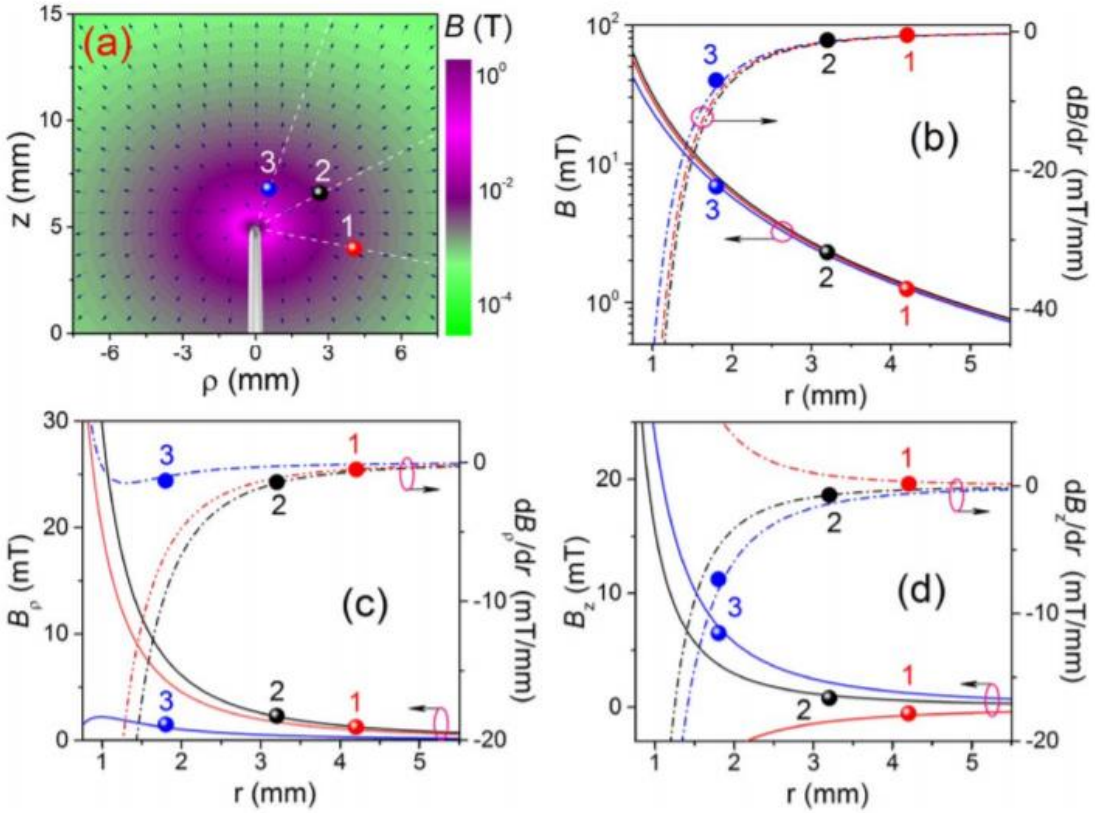

Fig. 3.9 (a) The map of the vectorial properties of the magnetic field (arrows) and its magnitude (color coding) induced by a uniformly magnetized needle (also shown). The dashed lines show the lines connecting the points where the field was measured in experiments with the tip of the magnetized needle. (b) The magnitude of the magnetic field B (circles and solid lines) and the radial part of its gradient, $\partial B/\partial r$ (circles and dashed–dotted lines), as a function of the distance r: (circles) experiment and (solid and dashed–dotted lines) calculations. (c), (d) The radial and longitudinal components of the magnetic field, B_ρ (c) and B_z (d), shown by circles and solid lines, and the radial part of their gradients, $\partial B_\rho/\partial r$ (c) and $\partial B_z/\partial r$ (d), shown by circles and dashed–dotted lines as functions of the distance r: (circles) experiment and (solid lines) calculations (solid and dashed–dotted lines). Calculations are performed along the lines connecting the points where the field was measured in experiments with the tip of the magnetized needle (dashed lines in (a)).

The gradients of the B_ρ and B_z projections of the magnetic field are retrieved in these experiments from the components of the $\boldsymbol{G}$ vector, composed of two-point magnetic field readings, as described above. In three representative measurements performed with the fiber probe positioned at three different locations in the plane of Fig. 3.9 (a) at distances r_1 = 4.5 mm, r_2 = 3.2 mm, and r_3 = 1.8 mm from the tip of the needle, the $\boldsymbol{G}$ vector sampling gives $\boldsymbol{G}_1$ = (0.29, 0.34, 0.11) mT⁄mm, $\boldsymbol{G}_2$ = (−0.87, 0.66, −0.015) mT⁄mm, and $\boldsymbol{G}_3$ (−0.78, 2.7, −2.4) mT⁄mm. As can be seen from Figs. 3.9 (b)-(d), the results of these measurements, presented by circles, are in a perfect agreement with the calculations, shown by the solid lines for B, B_ρ and B_z and by the dashed–dotted lines for the radial parts of their gradients, $\partial B/\partial r$, $\partial B_\rho/\partial r$, and $\partial B_z/\partial r$. Small discrepancies between experimental results and calculations are attributed primarily to deviations of the needle from the cylindrical shape and inhomogeneities in needle magnetization.

To summarize this section, highly sensitive room-temperature vectorial magnetic-field gradiometry using ODMR in fiber-coupled NV centers in diamond was demonstrated. With a bulk NV-diamond magnetometer coupled to a pair of optical fibers integrated with a microwave transmission line, the differential ODMR measurements are implemented in both space and time, with magnetic-field gradient measurements supplemented with differential ODMR signal detection in the time domain, allowing efficient noise cancellation and providing a magnetic gradient sensitivity at the level of $10^{-7}\ \mathrm{nT}/\left(\mathrm{nm\ Hz}^{1/2}\right)$.

3.5 QUANTUM STEREOMAGNETOMETRY WITH A DUAL-CORE PHOTONIC-CRYSTAL FIBER

In sections 3.3 and 3.4, a dual-fiber regime for measuring magnetic field gradients against a high-field background was demonstrated. The spatial resolution of this technology is limited by the core-to-core separation of the two fibers, which is a function of the fiber diameter. In order to improve the spatial resolution of the probe, a smaller core-to-core separation is necessary, thereby necessitating either the use of smaller fibers or another technology all together. Commercially available index guided fibers are not a viable option due to their large diameters (on the order of ~125 μm) and lower acceptance angles. Thus a single fiber solution in the form of the dual-core PCF described in section 3.2 was employed to achieve the requisite higher spatial resolution.

This type of PCF, known as a "holey fiber," functions in much the same way as a step-index fiber. The periodic microstructured cladding creates a lower effective index of refraction in the cladding region than in the core region [70-72]. This property enhances the index contrast, and hence the numerical aperture (NA) of these kind of fibers. The NA is related to the acceptance angle θ_a, the core index of refraction n_{co}, and the cladding index n_{cl} via the relation $NA = \sqrt{n_{co}^2 - n_{cl}^2} = \sin\theta_a$. The NA of PCFs can be much higher than the NA in a commercial non-microstructured fiber [73]. The acceptance angle of these fibers is therefore larger, and they are able to collect light from larger angles than a standard index-guided fiber. However, the signal collected from spatially incoherent light sources like an NVD tends to fall as a function of decreasing

core diameter. This is because the fraction of signal collected within the acceptance angle of the fiber is related to the number of spatial modes that the fiber can accept. The number of modes M at a given wavelength λ, fiber core diameter d, and numerical aperture NA is described in Eq. 3.13 [70]:

$$M \approx \frac{\left[\frac{\pi d}{\lambda} NA\right]^2}{2} \quad (M \geq 1) \tag{3.13}$$

In Eq. 3.13, it is obvious that the larger NA of a photonic crystal fiber results in more guided modes at a fixed core diameter. Thus a PCF can operate with a smaller core diameter than an index-guided fiber without sacrificing signal collection efficiency. This has been exploited in previous work to enhance the signal from NVDs coupled to a small core diameter PCF [74].

Due to the core-to-core separation of 6 μm, the dual-core PCF probe described in section 3.2 is able to characterize weak magnetic fields at ultra-high spatial resolution in a room-temperature environment. This dual-core PCF NVD gradiometer combines all of the advantages of the dual-fiber NVD gradiometer demonstrated in sections 3.3-3.4 into a monolithic biocompatible package that is capable of discriminating weak, spatially localized field features against a high-field background.

A magnetic field gradient is calculated in the same manner as in sections 3.3-3.4 by collecting an ODMR spectrum from two distinct locations on the NVD surface within the proximity of the two cores of the dual-core PCF. A beam splitter (Fig. 3.10) is used to simultaneously couple 5 mW of the 532 nm second-harmonic output of a cw Nd:YAG laser into both channels [right inset Fig. 3.10] of the dual-core PCF NVD probe. A microwave wire wrapped around the probe tip provides modulated microwave excitation

necessary for lock-in assisted ODMR measurements. The PL signal from both cores is imaged onto a photodiode coupled to a lock-in amplifier that is referenced to the microwave modulation frequency.

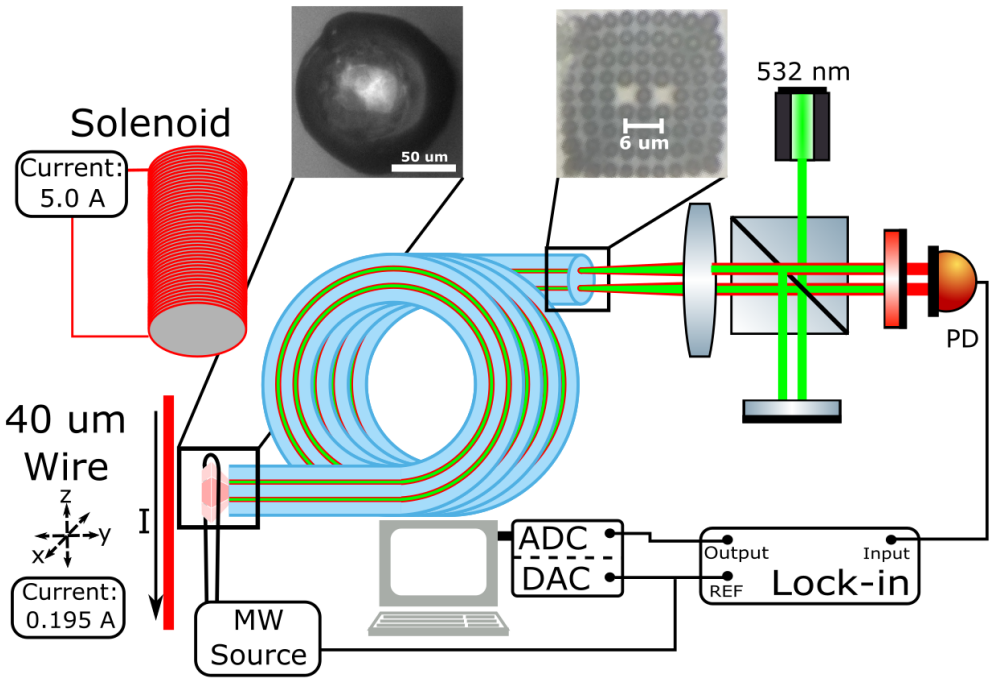

Fig. 3.10 Gradiometer setup consisting of a 300 mW frequency doubled Nd:YAG laser and a dual-core PCF NVD gradiometer probe with a core-to-core separation of 6 µm. Using a beam splitting optical regime that allows for independent spatial control of each beam's focal spot on the PCF, 5 mW of laser power is coupled into both cores of the PCF. AM/FM microwave excitation (MW Source) is delivered by a two-wire transmission line wrapped around the tip of the fiber-probe. PL signal from the probe is collected using a photodiode (PD) coupled to a lock-in amplifier referenced to the AM/FM modulation frequency and analyzed with a 14-bit ADC. A bias field from a custom solenoid supplied with 5 A of current is used to induce splitting of the ODMR peaks in order to aid data analysis. A 40 µm copper wire supplied with 195 mA (I) provides the field under study and is translated step-wise in approximately 25 µm increments in the x-z plane at a fixed distance from the wire of approximately 104 µm in the y-axis.

The magnetic field sensitivity of the probe is measured using the noise trace technique described in section 3.4 [41] by amplitude modulating (AM) the PL signal from one core with variable width FM microwave excitation centered at the point of highest slope on one peak in the ODMR spectrum (Fig. 3.11 (a)-(b)). The calculated magnetic field sensitivities were approximately 170 $\mathrm{nT}/\sqrt{\mathrm{Hz}}$ and 360 $\mathrm{nT}/\sqrt{\mathrm{Hz}}$ for core 1 and core 2 respectively.

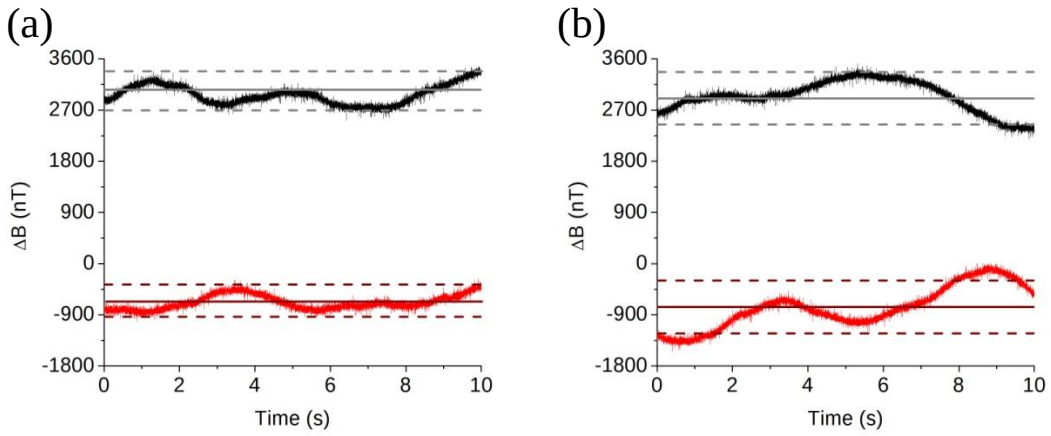

Fig. 3.11 Magnetic field sensitivities measured using the noise trace technique, corresponding to a magnetic field sensitivity of (a) 170 $\mathbf{nT}/\sqrt{\mathbf{Hz}}$ and (b) 360 $\mathbf{nT}/\sqrt{\mathbf{Hz}}$ measured with core 1 and core 2 respectively. Solid straight line indicates average PL amplitude, dashed straight line indicates standard deviation of PL amplitude.

ODMR spectra from each core are obtained by amplitude modulating the PL signal of that core with a 100 Hz AM microwave source swept in frequency between 2.6 GHz and 3.1 GHz and coupling the PD output to a lock-in amplifier referenced to the

AM frequency. The output of the lock-in amplifier is collected by the ADC and plotted versus microwave frequency to generate the ODMR spectrum. A static bias field from a custom built solenoid driven with 5 Amps at a fixed distance from the probe tip is provided to separate the ODMR peaks in the ODMR spectrum by a degree sufficient to allow analysis of each peak. The eight ODMR peaks in the ODMR spectrum are each fit with a Lorentzian function in order to determine the central frequency of each peak. These frequencies are used in Eqs. 3.3-3.7 to determine the magnitude and direction of the applied magnetic field measured by each core. An ODMR spectrum was measured through with cores in order to characterize the static bias field in the absence of any contributions from the wire. The bias field was found to have a magnitude of 6062 ± 3 μT measured by the first core of the gradiometer probe and a magnitude of 6083 ± 3 μT measured by the second core, corresponding to a calculated cross-core gradient of 3.5 ± 0.5 μT/μm induced by the bias field. Given the presence of a measurable magnetic field gradient induced by the bias solenoid, it is important to exclude all orders of the bias field contribution to the magnetic field gradient from the gradient induced by the wire alone. Because the location and orientation of the bias field is fixed with respect to the NVD on the probe tip, the contribution from the bias field is cancelled by subtracting out the bias field measurements from measurements in the presence of both the bias field and the wire field. Thus ODMR spectra are recorded with both cores in the presence of both field sources over a 4 by 4 grid of points in the x-z plane at a fixed distance in the y-axis. One additional measurement is made with both cores in close proximity to the

wire in the y-axis. ODMR spectra at this location and at one point in the 4 by 4 grid are compared in Fig. 3.12 (a)-(b).

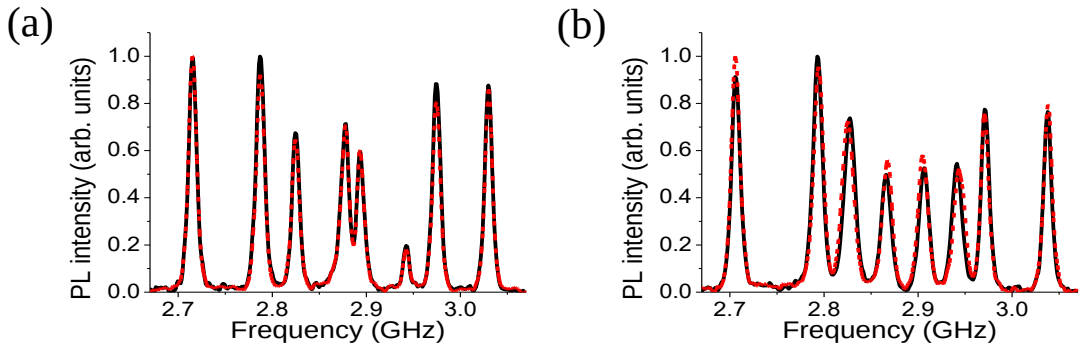

Fig 3.12 ODMR spectra recorded at (a) 104 ± 2 μm and (b) 47 ± 0.3 μm radial separation from the wire with core 1 (solid black curves) and core 2 (dashed red curves).

The total magnetic field magnitude and direction is calculated from the ODMR spectra, and the contribution of the bias field is subtracted out. The radial displacement ρ of each measurement point is calculated from the measured field value by using the equation the following equation for the magnetic field of a current carrying wire:

$$B = \frac{\mu_0 I}{2\pi\rho} \tag{3.14}$$

In Eq. 3.14, B represents the scalar magnetic field magnitude, μ_0 corresponds to the permeability of free space, I is the wire current of 195 mA, and ρ is the radial displacement of the measurement point from the wire. The calculated magnetic field of the wire measured from core 1 (solid black curve, Fig. 3.12 (a)) was 371 ± 9 μT and

from core 2 (dashed red curve, Fig. 3.12 (a)) was 362 ± 7 μT, corresponding to a radial probe displacement of 104 ± 2 μm from the wire. The calculated magnetic field of the wire measured from core 1 (solid black curve, Fig. 3.12 (b)) was 824 ± 7 μT and from core 2 (dashed red curve, Fig. 3.12 (b)) was 818 ± 8 μT, corresponding to a radial probe displacement of 47 ± 0.3 μm from the wire. Given the translational symmetry of the field of a current carrying wire, a z-axis field-profile obtained by averaging the fields along the z-axis is used to measure the scalar magnetic field gradient that exists between measurements made by core 1 (open circles, Fig. 3.13 (a)) and core 2 (filled circles, Fig. 3.13 (a)) at each step in the x-axis. The measured cross-core scalar gradient was 3.6 ± 5.7 μT/μm (red circles, Fig. 3.13 (a)), 3.2 ± 1.9 μT/μm (orange circles, Fig. 3.13 (a)), 2.5 ± 1.7 μT/μm (green circles, Fig. 3.13 (a)), and 2.1 ± 1.3 μT/μm (blue circles, Fig. 3.13 (a)) for probe positions of (0 μm,104 μm), (26 μm,108 μm), (53 μm,115 μm), and (81 μm,109 μm) in the x-y plane respectively. The locations of these measurements in the x-y plane are calculated using the full 3-D vector magnetic field data extracted from the ODMR spectra at each point in the vector field equation of a wire:

$$B_x\hat{x} + B_y\hat{y} = \frac{\mu_0 I}{2\pi}\left(-\hat{x}\frac{y}{x^2+y^2} + \hat{y}\frac{x}{x^2+y^2}\right) \tag{3.15}$$

In Eq. 3.15 B_x and B_y are the measured x and y field components of the wire, and $\hat{x}$ and $\hat{y}$ are the unit vectors in the direction of the x-axis and y-axis. A scalar gradient along the radial axis was also calculated using both cores by taking finite differences between the magnetic field values at each of the points in Fig. 3.13 (a) divided by their radial separation and plotted versus radial displacement, and was found to obey the appropriate $-1/\rho^2$ dependence described by the fitting function (grey dashed line, Figs. 3.13 (b)-(c)).

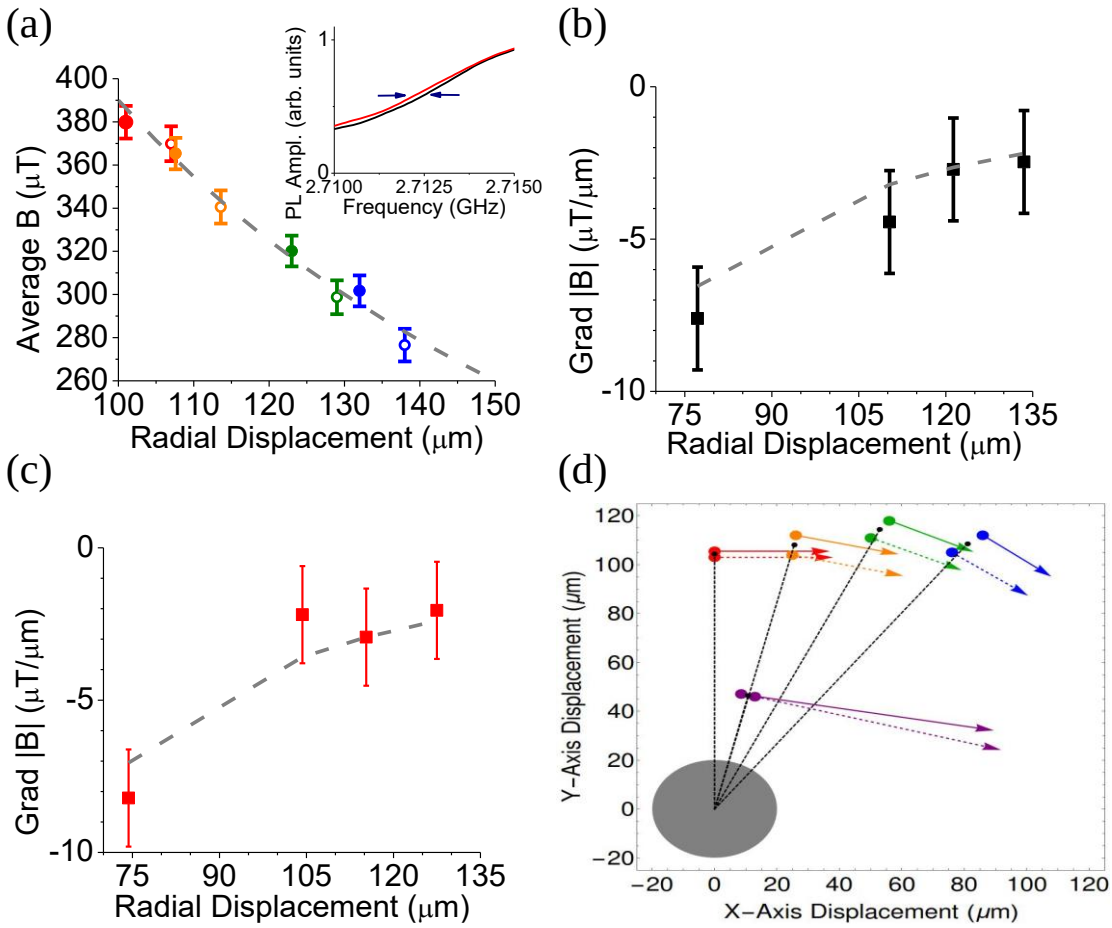

Fig. 3.13 (a) z-axis average scalar magnetic field values versus radial displacement measured with core 1 (open circles) and core 2 (filled circles). Data points colored red, orange, green, and blue represent magnetic field measurements performed with the probe at (x,y) locations (0 μm,104 μm), (26 μm,108 μm), (53 μm,115 μm), and (81 μm,109 μm) in the x-y plane respectively. Wire field fit as a function of radial displacement of probe represented by dashed grey curve. Inset figure demonstrates separation in ODMR peaks (blue arrows) between core 1 (black curve) and core 2 (red curve) for measurements taken at (26 μm, 108 μm). (b), (c) Radial magnetic field gradient measured by core 1 (black squares) and core 2 (red squares). Gradient of wire field fit as a function of radial displacement of probe represented by dashed grey curve. (d) Graph of scaled magnetic field vectors measured by core 1 (solid arrows) and core 2 (dashed arrows). Vector colors correspond to measurement locations described in (a), with the addition of the color violet corresponding to a measurement at the (x, y) location of (10 μm, 46 μm). Location of measurement points measured in μm displacement from scale model of wire (grey disk), colored circles represent location of measurement points. Current flows through wire into the page. Black dashed lines are radial separation between center of wire and approximate position of probe (black circles).

If the location of two measurement points is within a standard error in radial displacement from the source, the scalar gradient fails to be an effective tool at measuring an inhomogeneous field with high resolution, as seen in measurements in (red circles, Fig. 3.13 (a)). However, a vector field measurement can often overcome this limitation because the field at points equidistant from an inhomogeneous source can still have measurably different vector components. A z-axis profile of the magnetic vector field around the wire demonstrates the utility of vector measurements in measuring a field with high resolution. In Fig. 3.13 (d), the violet vector arrows corresponding to the magnetic field vectors associated with the measurement in Fig. 3.12 (b) lie within an error in position of each other but have measurably different components (Bx,By,Bz): (810±9 μT,-148±8 μT,-10±6 μT) and (788±9 μT,-218±8 μT,3±6 μT) for vectors measured by core 1 in (solid curves, Fig. 3.12 (b)) and core 2 in (dashed curves Fig. 3.12 (b)) respectively.

To summarize this section, a PCF-platform monolithic magnetic vector gradiometer with 170 $\mathrm{nT}/\sqrt{\mathrm{Hz}}$ of magnetic field sensitivity capable of measuring magnetic field gradients with 6 μm resolution and accuracies of up to 10 μT in the presence of a bias field three orders of magnitude larger than the field under study was demonstrated.

4. CONCLUSION

The ultimate objective of this research is to create minimally invasive biocompatible fiber probes for *in vivo* temperature and magnetic field diagnostics. To that end, a step by step guide to the fabrication of ultra-compact NVD fiber-optic thermometers, magnetometers, and gradiometers has been presented; their unique properties have been demonstrated and these probes have been tested in real world environments where high spatial resolution and high sensitivity are requisite.

A high accuracy fiber-optic thermometer was developed by incorporating an NVD onto the tip of an optical fiber with integrated microwave transmission lines. The NVD was interrogated optically through the fiber and an ODMR measurement regime was used to make temperature measurements and demonstrate an accuracy of up to 20 mK. By decreasing the diameter of the NVD used to create the probe, it is possible to produce a fiber-optic thermometer capable of performing temperature measurements with a spatial resolution on the scale of 30 μm. Resolutions on this order are necessary to determine temperature gradients across individual cells in a living tissue.

Dual-fiber magnetic gradiometer probes with a maximum sensitivity of 40 $\mathrm{nT}/\sqrt{\mathrm{Hz}}$ were developed by attaching a single bulk NVD to the tip of two optical fibers with an integrated microwave transmission line. The NVD was interrogated optically through both fibers using the ODMR technique in order to measure the magnetic field at two points on the diamond. These measurements were used to calculate magnitude and direction of the magnetic field gradient across the diamond, allowing for magnetic gradient measurements with 480 μm spatial resolution.

The demonstrated magnetic field gradient measurements are free of spatially homogeneous magnetic field noise. Elimination of temporal noise has also been demonstrated. These gradient measurements allow for discrimination of weak magnetic fields against magnetically noisy environments inherent to the *in vivo* nature of the desired realm of applications.

Finally, a dual-core PCF NVD gradiometer with a maximum sensitivity of approximately 170 $\mathrm{nT}/\sqrt{\mathrm{Hz}}$ and a 6 micron spatial resolution was demonstrated. This probe presents a convergence of ongoing efforts towards the development of a high-sensitivity, high spatial resolution vector stereomagnetometer in a monolithic, biocompatible platform.

REFERENCES

[1] V. A. Vaguine, D. A. Christensen, J. H. Lindley, and T. E. Walston, “Multiple sensor optical thermometry system for application in clinical hyperthermia,” IEEE Transactions on Biomedical Engineering, BME-31, 168-172 (1984)

[2] A. Katzir, H.F. Bowman, Y. Asfour, A. Zur, and C.R. Valeri, "Infrared fibers for radiometer thermometry in hypothermia and hyperthermia treatment," IEEE Transactions on Biomedical Engineering, BME-36, 634-637 (1989)

[3] A. Zur and A. Katzir, "Fiber optic distributed thermal sensor," Applied Physics Letters 53, 2474-2476 (1988)

[4] A. Katzir, F. Bowman, Y. Asfour, A. Zur, and C. R. Valery, "Infrared fiber optics for thermometry in microwave", Applied Physics Letters 53, 1877-1879 (1988)

[5] Y. J. Rao, D. J. Webb, D. A. Jackson, L. Zhang, and I. Bennion, “Optical in-fiber bragg grating sensor systems for medical applications,” Journal of Biomedical Optics 3, 38-44 (1998)

[6] D. Polito, M. A. Caponero, A. Polimadei, P. Saccomandi, C. Massaroni, S. Silvestri, and E. Schena, “A needle-like probe for temperature monitoring during laser ablation based on FBG: Manufacturing and characterization” Journal of Medical Devices 9, 041006 (2015)

[7] G. Allegrettia, P. Saccomandia, F. Giurazzab, M. A. Caponeroc, G. Frauenfelderb, F. M. Di Matteod, B. Beomonte Zobelb, S. Silvestria, E. Schenaa, “Magnetic resonance-based thermometry during laser ablation on ex-vivo swine pancreas and liver,” Medical Engineering and Physics 37, 631-641 (2015)

[8] Z. Zhang, K. Grattan, A. Palmer, "Fiber-optic high-temperature sensor based on the fluorescence lifetime of alexandrite," Review of Scientific Instruments 63, 3869-3873 (1992)

[9] H. Berthou and C. K. Jörgensen, "Optical-fiber temperature sensor based on upconversion-excited fluorescence," Optics Letters 15, 1100-1102 (1990)

[10] J. C. Chen, J. A. Moriarty, J. A. Derbyshire, R. D. Peters, J. Trachtenberg, S. D. Bell, J. Doyle, R. Arrelano, G. A. Wright, R. M. Henkelman, R. S. Hinks, S. Lok, A. Toi, and W. Kucharczyk, "Prostate Cancer: MR Imaging and Thermometry during Microwave Thermal Ablation-Initial Experience," Radiology 214, 290-297 (2000)

[11] T. M. Buzug, S. Schumann, L. Pfaffmann, U. Reinhold, and J. Ruhlmann, "Functional Infrared Imaging for Skin-Cancer Screening," Engineering in Medicine and Biology Society, 28th Annual International Conference of the IEEE, 2766-2769 (2006)

[12] A. Weis, "Optically pumped alkali magnetometers for biomedical applications," Europhysics News 43, 20-23 (2012)

[13] C. Affolderbach, M. Stähler, S. Knappe, and R. Wynands, "An all-optical, high-sensitivity magnetic gradiometer," Applied Physics B 75, 605-612 (2002)

[14] G. Bison, R. Wynands, and A. Weis, "Dynamical mapping of the human cardiomagnetic field with a room-temperature, laser-optical sensor," Optics Express 11, 904-909 (2003)

[15] G. Bison, R. Wynands, and A. Weis, "A laser-pumped magnetometer for the mapping of human cardiomagnetic fields," Applied Physics B 76, 325-328 (2003)

[16] G. Davies, M. F. Hamer, “Optical Studies of the 1.945 eV Vibronic Band in Diamond,” Proceedings of the Royal Society A 348, 285-298 (1976)

[17] J. H. N. Loubser, J. A. van Wyk, “Electron spin resonance in the study of diamond,” Reports on Progress in Physics 41, 1201-1249 (1978)

[18] S. Zhou, S. Jiang, X. Wei, Y. Chen, C. Duan, and M. Yin, “Optical thermometry based on upconversion luminescence in Yb^{3+}/Ho^{3+} co-doped $NaLuF_4$,” Journal of Alloys and Compounds 588, 654-657 (2014)

[19] I. V. Fedotov, S. Blakley, E. E. Serebryannikov, N. A. Safronov, V. L. Velichansky, M. O. Scully, and A. M. Zheltikov, “Fiber-based thermometry using optically detected magnetic resonance,” Applied Physics Letters 105, 261109 (2014)

[20] K. Sokolov, “Nanotechnology: Tiny thermometers used in living cells,” Nature 500, 36-37 (2013)

[21] J. M. Taylor, P. Cappellaro, L. Childress, L. Jiang, D. Budker, P.R. Hemmer, A. Yacoby, R. Walsworth, and M.D. Lukin, “High-sensitivity diamond magnetometer with nanoscale resolution,” Nature Physics 4, 810-816 (2008)

[22] S. M. Blakley, I. V. Fedotov, S. Ya. Kilin, and A. M. Zheltikov, “Room-temperature magnetic gradiometry with fiber-coupled nitrogen-vacancy centers in diamond,” Optics Letters 40, 16 3727-3730 (2015)

[23] S. J. Bending, “Local magnetic probes of superconductors,” Advances in Physics 45, 4 449-535 (1999)

[24] M. V. Romalis, “Chip-scale magnetometers,” Nature Photonics 1, 613-614 (2007)

[25] I. V. Fedotov, L. V. Doronina-Amitonova, D. A. Sidorov-Biryukov, N. A. Safronov, S. Blakley, A. O. Levchenko, S. A. Zibrov, A. B. Fedotov, S. Ya. Kilin, M. O. Scully, V. L. Velichansky, and A. M. Zheltikov, "Fiber-optic magnetic-field imaging," Optics Letters 39, 24 6954-6957 (2014)

[26] J. R. Maze, P. L. Stanwix, J. S. Hodges, S. Hong, J. M. Taylor, P. Cappellaro, L. Jiang, M. V. Gurudev Dutt, E. Togan, A. S. Zibrov, A. Yacoby, R. L. Walsworth, and M. D. Lukin, "Nanoscale magnetic sensing with an individual electronic spin in diamond," Nature 455, 644-647 (2008)

[27] S. M. Blakley, Y, I. V. Fedotov, L. V. Amitonova, E. E. Serebryannikov, H. Perez, S. Ya. Kilin, and A. M. Zheltikov, "Fiber-optic vectorial magnetic-field gradiometry by a spatiotemporal differential optical detection of magnetic resonance in nitrogen–vacancy centers in diamond," Optics Letters 41, 9 2057-2060 (2016)

[28] G. Balasubramanian, I. Y. Chan, R. Kolesov, M. Al-Hmoud, J. Tisler, C. Shin, C. Kim, A. Wojcik, P. R. Hemmer, A. Krueger, T. Hanke, A. Leitenstorfer, R. Bratschitsch, F. Jelezko, and J. Wrachtrup, "Nanoscale imaging magnetometry with diamond spins under ambient conditions," Nature 455, 648-651 (2008)

[29] D. Le Sage, K. Arai, D. R. Glenn, S. J. DeVience, L. M. Pham, L. Rahn-Lee, M. D. Lukin, A. Yacoby, A. Komeili, and R. L. Walsworth, "Optical magnetic imaging of living cells," Nature 496, 486-489 (2013)

[30] G. L. Eesley, "Coherent Raman Spectroscopy," Pergamon, Oxford (1981)

[31] S. A. J. Druet and J. P. E. Taran, "Cars Spectroscopy," Progress in Quantum Electronics 7, 1-72 (1981)

[32] A. M. Zheltikov and N. I. Koroteev, “Coherent four-wave mixing in excited and ionized gas media: four-photon spectrochronography, ellipsometry, and nonlinear-optical imaging of atoms and ions,” Physics-Uspekhi 42, 321-351 (1999)

[33] A. D. Kersey, “A Review of Recent Developments in Fiber Optic Sensor Technology,” Optical Fiber Technology 2, 291-317 (1999)

[34] B. Lee, “Review of the present status of optical fiber sensors,” Optical Fiber Technology 9, 57-79 (2003)

[35] V. M. Acosta, E. Bauch, M. P. Ledbetter, A. Waxman, L.-S. Bouchard, and D. Budker, “Temperature Dependence of the Nitrogen-Vacancy Magnetic Resonance in Diamond,” Physical Review Letters 104, 070801 (2010)

[36] G. Kucsko, P. C. Maurer, N. Y. Yao, M. Kubo, N. J. Noh, P. K. Lo, H. Park, and M. D. Lukin, “Nanometre-scale thermometry in a living cell,” Nature 500, 54-58 (2013)

[37] I.V. Fedotov, N.A. Safronov, Yu.G. Ermakova, M.E. Matlashov, D.A. Sidorov-Biryukov, A.B. Fedotov, V.V. Belousov, and A.M. Zheltikov, “Fiber-optic control and thermometry of single-cell thermosensation logic,” Scientific Reports 5, 15737 (2015)

[38] I. V. Fedotov, L. V. Doronina-Amitonova, A. A. Voronin, A. O. Levchenko, S. A. Zibrov, D. A. Sidorov-Biryukov, A. B. Fedotov, V. L. Velichansky, and A. M. Zheltikov, “Electron spin manipulation and readout through an optical fiber,” Scientific Reports 4, 5362 (2014)

[39] D. A. Redman, S. Brown, R. H. Sands, and S. C. Rand, “Spin dynamics and electronic states of N-V centers in diamond by EPR and four-wave-mixing spectroscopy,” Physical Review Letters 67, 3420-3423 (1991)

[40] I. V. Fedotov, N. A. Safronov, Yu. A. Shandarov, A. A. Lanin, A. B. Fedotov, S. Ya. Kilin, K. Sakoda, M. O. Scully, and A. M. Zheltikov, "Guided-wave-coupled nitrogen vacancies in nanodiamond-doped photonic-crystal fibers," Applied Physics Letters 101, 031106 (2012)

[41] R. S. Schoenfeld and W. Harneit, "Real Time Magnetic Field Sensing and Imaging Using a Single Spin in Diamond," Physical Review Letters 106, 030802 (2011)

[42] K. Deisseroth, "Optogenetics," Nature Methods 8, 26-29 (2011)

[43] G. Miesenböck, "The Optogenetic Catechism," Science 326, 395-399 (2009)

[44] M. R. Warden, J. A. Cardin, and K. Deisseroth. "Optical Neural Interfaces," Annual Review of Biomedical Engineering 16, 103–129 (2014)

[45] L. Fenno, O. Yizhar, and K. Deisseroth, "The Development and Application of Optogenetics," Annual Review of Neuroscience 34, 389-412 (2011)

[46] I. Diester, M. T. Kaufman, M. Mogri, R. Pashaie, W. Goo, O. Yizhar, C. Ramakrishnan, K. Deisseroth, and K. V. Shenoy, "An optogenetic toolbox designed for primates," Nature Neuroscience 14, 387-397 (2011)

[47] F. Zhang, L. Wang, M. Brauner, J. F. Liewald, K. Kay, N. Watzke, P. G. Wood, E. Bamberg, G. Nagel, A. Gottschalk, and K. Deisseroth, "Multimodal fast optical interrogation of neural circuitry," Nature 466, 633-639 (2007)

[48] F. Zhang, V. Gradinaru, A. R. Adamantidis, R. Durand, R. D. Airan, L. Lecea, and K. Deisseroth, "Optogenetic interrogation of neural circuits: technology for probing mammalian brain structures," Nature Protocols 5, 439-456 (2010)

[49] D. D. McKemy, W. M. Neuhausser, and D. Julius, “Identification of a cold receptor reveals a general role for TRP channels in thermosensation,” Nature 416, 52-58 (2002)

[50] H. Xu, I. S. Ramsey, S. A. Kotecha, M. M. Moran, J. A. Chong, D. Lawson, P. Ge, J. Lilly, I. Silos-Santiago, Y. Xie, P. S. DiStefano, R. Curtis, and D. E. Clapham, “TRPV3 is a calcium-permeable temperature-sensitive cation channel,” Nature 418, 181-186 (2002)

[51] A. Moqrich, S. W. Hwang, T. J. Earley, M. J. Petrus, A. N. Murray, K. S. R. Spencer, M. Andahazy, G. M. Story, and A. Patapoutian, “Impaired Thermosensation in Mice Lacking TRPV3, a Heat and Camphor Sensor in the Skin,” Science 307, 1468-1472 (2005)

[52] A. Patapoutian, A. M. Peier, G. M. Story, and V. Viswanath, “ThermoTRP channels and beyond: mechanisms of temperature sensation,” Nature Reviews Neuroscience 4, 529-539 (2003)

[53] J. G. Bernstein, P. A. Garrity, and E. S. Boyden, “Optogenetics and thermogenetics: technologies for controlling the activity of targeted cells within intact neural circuits,” Current Opinion in Neurobiology 22, 61-71 2012

[54] G. M. Story, A. M. Peier, A. J. Reeve, S. R. Eid, J. Mosbacher, T. R. Hricik, T. J. Earley, A. C. Hergarden, D. A. Andersson, S. W. Hwang, P. McIntyre, T. Jegla, S. Bevan, and A. Patapoutian, “ANKTM1, a TRP-like Channel Expressed in Nociceptive Neurons, Is Activated by Cold Temperatures,” Cell 112, 819-829 (2003)

[55] E. O. Gracheva, N. T. Ingolia, Y. M. Kelly, J. F. Cordero-Morales, G. Hollopeter, A. T. Chesler, E. E. Sánchez, J. C. Perez, J. S. Weissman, and D. Julius, "Molecular basis of infrared detection by snakes," Nature 464, 1006-1011 (2010)

[56] C. Belmonte, J. A. Brock, and F. Viana, "Converting cold into pain," 196, 13-30 (2009)

[57] B. Nilius and G. Owsianik, "The transient receptor potential family of ion channels," Genome Biology 12, 218-228 (2011)

[58] T. G. Banke, S. R. Chaplan, and A. D. Wickenden, "Dynamic changes in the TRPA1 selectivity filter lead to progressive but reversible pore dilation," American Journal of Physiology Cell Physiology 298, C1457-C1468 (2010)

[59] D. E. Bath, J. R. Stowers, D. Hörmann, A. Poehlmann, B. J. Dickson, and A. D. Straw, "FlyMAD: rapid thermogenetic control of neuronal activity in freely walking *Drosophila*," Nature Methods 11, 756-762 (2014)

[60] Y. Zhao, S. Araki, J. Wu, T. Teramoto, Y. Chang, M. Nakano, A. S. Abdelfattah, M. Fujiwara, T. Ishihara, T. Nagai, and R. E. Campbell, "An Expanded Palette of Genetically Encoded Ca^{2+} Indicators," Science 333, 1888-1891 (2011)

[61] Yu. G. Ermakova, D. S. Bilan, M. E. Matlashov, N. M. Mishina, K. N. Markvicheva, O. M. Subach, F. V. Subach, I. Bogeski, M. Hoth, G. Enikolopov, and V. V. Belousov, "Red fluorescent genetically encoded indicator for intracellular hydrogen peroxide," Nature Communications 5, 5222 (2014)

[62] N. A. Safronov, I. V. Fedotov, Yu. G. Ermakova, M. E. Matlashov, D. A. Sidorov-Biryukov, A. B. Fedotov, V. V. Belousov, and A. M. Zheltikov, "Microwave-induced thermogenetic activation of single cells," Applied Physics Letters 106, 163702 (2015)

[63] T. Gaebel, M. Domhan, I. Popa, C. Wittmann, P. Neumann, F. Jelezko, J. R. Rabeau, N. Stavrias, A. D. Greentree, S. Prawer, J. Meijer, J. Twamley, P. R. Hemmer, and J. Wrachtrup, "Room-temperature coherent coupling of single spins in diamond," Nature Physics 2, 408-413 (2006)

[64] L. Childress, M. V. G. Dutt, J. M. Taylor, A. S. Zibrov, F. Jelezko, J. Wrachtrup, P. R. Hemmer, and M. D. Lukin, "Coherent Dynamics of Coupled Electron and Nuclear Spin Qubits in Diamond," Science 314, 281-285 (2006)

[65] M. V. G. Dutt, L. Childress, L. Jiang, E. Togan, J. Maze, F. Jelezko, A. S. Zibrov, P. R. Hemmer, and M. D. Lukin, "Quantum Register Based on Individual Electronic and Nuclear Spin Qubits in Diamond," Science 316, 1312-1316 (2007)

[66] I. Aharonovich, A. D. Greentree, and S. Prawer, "Diamond photonics," Nature Photonics 5, 397-405 (2011)

[67] A. Gruber, A. Dräbenstedt, C. Tietz, L. Fleury, J. Wrachtrup, and C. von Borczyskowski, "Scanning Confocal Optical Microscopy and Magnetic Resonance on Single Defect Centers," Science 276, 2012-2014 (1997)

[68] A. Dréau, M. Lesik, L. Rondin, P. Spinicelli, O. Arcizet, J.-F. Roch, and V. Jacques, "Avoiding power broadening in optically detected magnetic resonance of single NV defects for enhanced dc magnetic field sensitivity," Physical Review B 84, 195204 (2011)

[69] K. K. Khurana, E. L. Kepko, M. G. Kivelson, and R. C. Elphic, “Accurate determination of magnetic field gradients from four-point vector measurements,” IEEE Transactions on Magnetics 32, 5193-5205 (1996)

[70] J. C. Knight, T. A. Birks, and P. St. J. Russell, “Properties of photonic crystal fiber and the effective index model,” Journal of the Optical Society of America A 15, 748-752 (1998)

[71] P. St. J. Russell, "Photonic crystal fibers," Science 299, 358–362 (2003)

[72] P. St. J. Russell, “Photonic-crystal fibers,” Journal of Lightwave Technology 24, 4729–4749 (2006)

[73] W. J. Wadsworth, R. M. Percival, G. Bouwmans, J. C. Knight, T. A. Birks, T. D. Hedley, and P. St. J. Russell, “Very High Numerical Aperture Fibers,” IEEE Photonics Technology Letters 16, 843-845 (2004)

[74] I. V. Fedotov, N. A. Safronov, Yu. A. Shandarov, A. A. Lanin, A. B. Fedotov, S. Ya. Kilin, K. Sakoda, M. O. Scully, and A. M. Zheltikov, “Guided-wave-coupled nitrogen vacancies in nanodiamond-doped photonic-crystal fibers,” Applied Physics Letters 101, 031106 (2012)